



Giant spontaneous Hall effect in a nonmagnetic Weyl–Kondo semimetal

Sami Dzsaber^a, Xinlin Yan^a, Mathieu Taupin^a, Gaku Eguchi^a, Andrey Prokofiev^a, Toni Shiroka^{b,c}, Peter Blaha^d, Oleg Rubel^e, Sarah E. Grefe^f, Hsin-Hua Lai^f, Qimiao Si^f, and Silke Paschen^{a,f,1}

^aInstitute of Solid State Physics, Vienna University of Technology, 1040 Vienna, Austria; ^bLaboratorium für Festkörperphysik, ETH Zürich, 8093 Zurich, Switzerland; ^cPaul Scherrer Institut, 5232 Villigen PSI, Switzerland; ^dInstitute of Materials Chemistry, Vienna University of Technology, 1040 Vienna, Austria; ^eDepartment of Materials Science and Engineering, McMaster University, Hamilton, ON L8S 4L8, Canada; and ^fDepartment of Physics and Astronomy, Rice Center for Quantum Materials, Rice University, Houston, TX 77005

Edited by Allan H. MacDonald, University of Texas at Austin, Austin, TX, and approved January 19, 2021 (received for review June 26, 2020)

Nontrivial topology in condensed-matter systems enriches quantum states of matter to go beyond either the classification into metals and insulators in terms of conventional band theory or that of symmetry-broken phases by Landau's order parameter framework. So far, focus has been on weakly interacting systems, and little is known about the limit of strong electron correlations. Heavy fermion systems are a highly versatile platform to explore this regime. Here we report the discovery of a giant spontaneous Hall effect in the Kondo semimetal $Ce_3Bi_4Pd_3$ that is noncentrosymmetric but preserves time-reversal symmetry. We attribute this finding to Weyl nodes—singularities of the Berry curvature—that emerge in the immediate vicinity of the Fermi level due to the Kondo interaction. We stress that this phenomenon is distinct from the previously detected anomalous Hall effect in materials with broken time-reversal symmetry; instead, it manifests an extreme topological response that requires a beyond-perturbation-theory description of the previously proposed nonlinear Hall effect. The large magnitude of the effect in even tiny electric and zero magnetic fields as well as its robust bulk nature may aid the exploitation in topological quantum devices.

Weyl semimetal | Kondo effect | spontaneous Hall effect | preserved time-reversal symmetry

Exploring effects of topology (1–7) in weakly correlated condensed-matter systems has led to the identification of fundamentally new quantum phases and phenomena, including the spin Hall effect (8), protected transport of helical fermions (9), topological superconductivity (10), and large nonlinear optical response (11, 12). In the recently discovered Weyl semimetals, bulk three-dimensional (3D) Dirac cones describing massless relativistic quasiparticles are stabilized by breaking either inversion symmetry (IS) or time-reversal symmetry (TRS) (13). Key experiments in their identification have been angle-resolved photoemission spectroscopy (ARPES) (14–16) as well as magnetotransport measurements, providing evidence for the chiral anomaly (13, 17, 18)—charge pumping between a pair of Weyl nodes—via a large negative longitudinal magnetoresistance or, for nanostructures in high magnetic fields, Weyl orbits via quantum oscillation (19) or quantum Hall measurements (20). Whereas the perturbative effect of correlations on topological electronic states is already under broad investigation (21–24), a completely open question is how strong correlations drive either related or entirely new topological states (25–29). To uncover them experimentally, not only new materials but also alternative measurement techniques have to be found. For instance, to characterize the recently proposed Weyl–Kondo semimetals (30, 31) neither of the canonical probes for weakly interacting Weyl semimetals seems suitable: ARPES experiments still lack the ultrahigh resolution needed to resolve strongly renormalized bands and magnetotransport signatures of the chiral anomaly or Weyl orbits are expected to be suppressed by the reduced

quasiparticle velocities of strongly correlated materials (18). Our discovery of a giant spontaneous Hall effect in one such material not only identifies an ideal technique but also demonstrates that strong correlations can drive extreme topological responses, which we expect to trigger much further work.

The material we have investigated is the noncentrosymmetric and nonsymmorphic heavy fermion semimetal $Ce_3Bi_4Pd_3$ (30) that has recently been identified as a candidate Weyl–Kondo semimetal (30, 31). Its low-temperature specific heat contains a giant electronic $c = \Gamma T^3$ term that was attributed to electronic states with extremely flat linear dispersion (30), corresponding to a quasiparticle velocity v^* that is renormalized by a factor of 10^3 with respect to the Fermi velocity of a simple metal (30, 31). This boosts the electronic ΓT^3 term to the point that it even overshoots the Debye βT^3 term of acoustic phonons (30). To scrutinize this interpretation by other, more direct probes of topology is the motivation for the present work.

Results

We start by showing that $Ce_3Bi_4Pd_3$ is governed by the Kondo interaction and delineate the temperature and field range of Kondo coherence. The zero-field resistivity of $Ce_3Bi_4Pd_3$ increases weakly with decreasing temperature, whereas the nonmagnetic reference compound $La_3Bi_4Pd_3$ is metallic (Fig. 1A). This provides strong evidence that the semimetallic character of $Ce_3Bi_4Pd_3$ is due to the Kondo interaction. Below the single-ion Kondo temperature $T_K = 13$ K, identified by associating

Significance

States of matter are traditionally classified by their symmetry, as exemplified by the distinction between a solid and a liquid. Topological quantum phases, on the other hand, are harder to characterize, and still harder to identify. This is especially so in electronic systems with strong correlations. In this work, we uncover a purely electric-field-driven “giant” Hall response—orders of magnitude above expectation—in one such material and propose a mechanism whereby it is driven by strong correlations. Our results will enable the identification of electronic topological states in a broad range of strongly correlated quantum materials and may trigger efforts toward their exploitation in robust quantum electronics.

Author contributions: S.D., Q.S., and S.P. designed the research; S.D., X.Y., M.T., G.E., A.P., T.S., P.B., O.R., S.E.G., and H.-H.L. performed the research; S.D., M.T., and T.S. analyzed the data; and S.D., Q.S., and S.P. wrote the paper.

The authors declare no competing interest.

This article is a PNAS Direct Submission.

This open access article is distributed under Creative Commons Attribution-NonCommercial-NoDerivatives License 4.0 (CC BY-NC-ND).

¹ To whom correspondence may be addressed. Email: paschen@ifp.tuwien.ac.at.

This article contains supporting information online at <https://www.pnas.org/lookup/suppl/doi:10.1073/pnas.2013386118/-DCSupplemental>.

Published February 19, 2021.

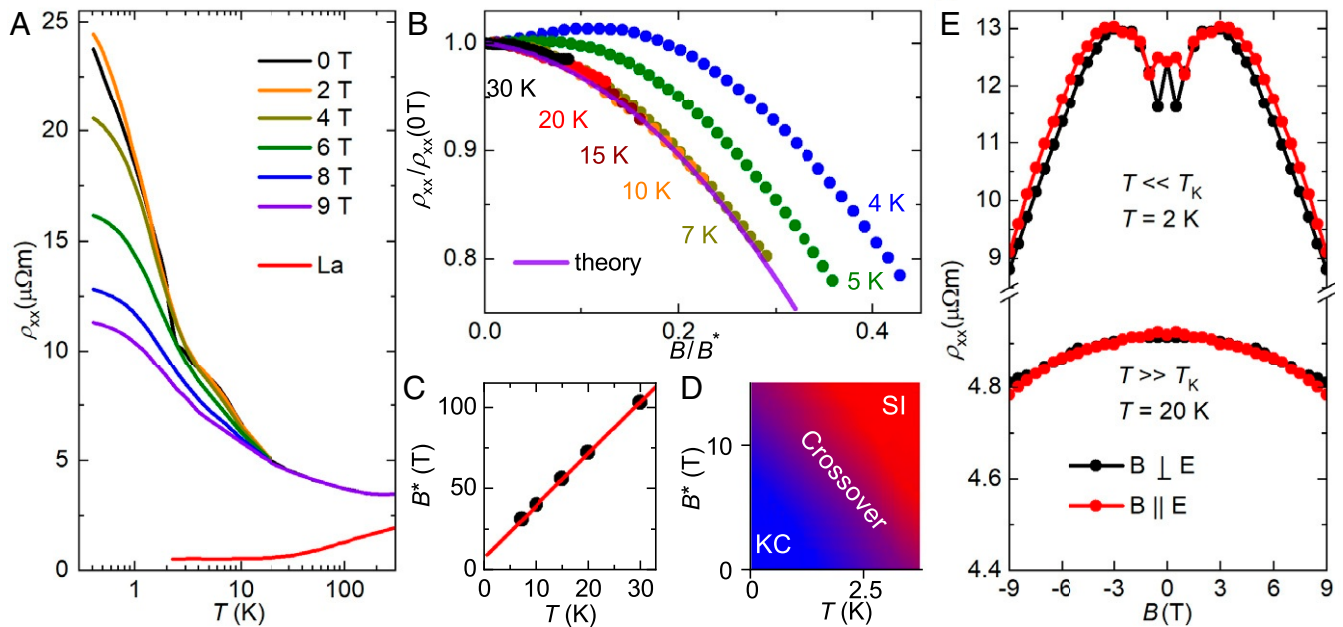


Fig. 1. Electrical resistivity and magnetoresistance of $\text{Ce}_3\text{Bi}_4\text{Pd}_3$. (A) Temperature-dependent electrical resistivity ρ_{xx} of $\text{Ce}_3\text{Bi}_4\text{Pd}_3$ in various magnetic fields applied perpendicular to the electric field ($B \perp E$, transverse magnetoresistance) and of the nonmagnetic reference compound $\text{La}_3\text{Bi}_4\text{Pd}_3$ in zero field (red). The feature in the 0 T data of $\text{Ce}_3\text{Bi}_4\text{Pd}_3$ near 3 K is due to the onset of the spontaneous Hall effect (Fig. 2A), which leaves a finite imprint on ρ_{xx} because of the giant Hall angle (SI Appendix, section I H) and because of slight contact misalignment (SI Appendix, section I A). (B) Transverse magnetoresistance scaled to its zero-field value vs. scaled magnetic field B/B^* , showing the collapses of data above 7 K onto the universal scaling (32) (violet) expected for an $S = 1/2$ Kondo impurity system in the incoherent regime and a breakdown of the scaling for temperatures below 7 K (shown here by using B^* from the linear fit in C—also, other choices of B^* cannot achieve scaling). (C) Scaling field B^* , as determined in B, vs. temperature, showing a linear-in- T behavior as expected for a Kondo system in the single-impurity regime. Fitting $B^* = B_0^*(1 + T/T^*)$ to the data (red straight line) yields $B_0^* = 10$ T and $T^* = 2.5$ K. (D) Temperature-field phase diagram displaying the single impurity (SI) and Kondo coherent (KC) regime as derived in C. (E) Transverse (black) and longitudinal (red, $B \parallel E$) magnetoresistance for temperatures well below (Top) and well above T_K (Bottom). The data were symmetrized to remove any spurious Hall resistivity contribution and mirrored on the vertical axis for clarity.

the material's temperature-dependent entropy with a spin 1/2 ground state doublet of the Ce $4f^1$ wavefunction split by the Kondo interaction (30), a broad shoulder in the resistivity at about 7 K signals the cross-over to a Kondo coherent state (Fig. 1A). As shown in what follows, this is further supported by our magnetoresistance measurements (Fig. 1B and C).

Transverse magnetoresistance isotherms (Fig. 1B) in the incoherent regime between 7 and 30 K display the universal scaling typical of Kondo systems (33, 34): $\rho_{xx}/\rho_{xx}(0\text{ T})$ vs. B/B^* curves all collapse onto the theoretically predicted curve for an $S = 1/2$ Kondo impurity system (32), provided a suitable scaling field B^* is chosen. The resulting B^* is linear in temperature (Fig. 1C). Fitting $B^* = B_0^*(1 + T/T^*)$ to the data (red straight line) yields $B_0^* = 10$ T and $T^* = 2.5$ K, which may be used as estimates of the field and temperature below which the system is fully Kondo coherent (blue area in Fig. 1D). Below 7 K, the scaling fails (Fig. 1B), as expected when crossing over from the incoherent to the Kondo coherent regime.

Before presenting our Hall effect results we show that, as anticipated, the chiral anomaly cannot be resolved in the Kondo coherent regime. We find that, at 2 K, the longitudinal and transverse magnetoresistance traces essentially collapse (Fig. 1E, Top). Because the amplitude c_a of the chiral anomaly, being inversely proportional to the density of states (18), is expected to scale as $c_a \propto (v^*)^3$, it is severely suppressed by the strong correlations. The fact that, also at high temperatures, we do not observe signatures of the chiral anomaly (Fig. 1E, Bottom) is consistent with our bandstructure calculations (to be presented later; see Fig. 4A), which reveal that the uncorrelated bandstructure contains Weyl nodes only far away (> 100 meV) from the Fermi level.

Our key observation, presented next, is a spontaneous (non-linear, as will be discussed later) Hall effect which appears in $\text{Ce}_3\text{Bi}_4\text{Pd}_3$ as full Kondo coherence is established below T^* (Fig. 2A). The corresponding spontaneous Hall conductivity σ_{xy} reaches a considerable fraction of the quantum of 3D conductivity (Fig. 2B). The experiment, using a pseudo-AC (alternating current) mode (Materials and Methods), was not only carried out in zero external magnetic field but also without any sample pre-magnetization process. Hall contact misalignment contributions were corrected for (SI Appendix, section I A and Figs. S1 and S2) and, thus, can also not account for the effect. Moreover, being in the Kondo coherent regime, the local moments should be fully screened by the conduction electrons. The resulting paramagnetic state is evidenced by the absence of phase transition anomalies in magnetization and specific heat measurements (SI Appendix, sections II B and C and Figs. S11 and S12), as well as by state-of-the-art zero-field (ZF) muon spin rotation (μSR) experiments. The latter reveal an extremely small electronic relaxation rate that is temperature-independent between 30 K and 250 mK (Fig. 2C; for two fully overlapping representative spectra, one well above and one well below T^* , see SI Appendix, section II A and Fig. S10). This is unambiguous evidence that, in the investigated temperature range and in particular across T^* , TRS is preserved in $\text{Ce}_3\text{Bi}_4\text{Pd}_3$. In conjunction with the giant spontaneous Hall effect this observation is striking—we are not aware of any other 3D material with preserved TRS that has shown a spontaneous Hall effect.

We also measured the Hall effect in finite applied magnetic fields. We observe that the field-dependent Hall resistivity isotherms, $\rho_{xy}(B)$, are fundamentally different below (Fig. 3A) and above T^* (Fig. 3B). Whereas above T^* , ρ_{xy} shows simple

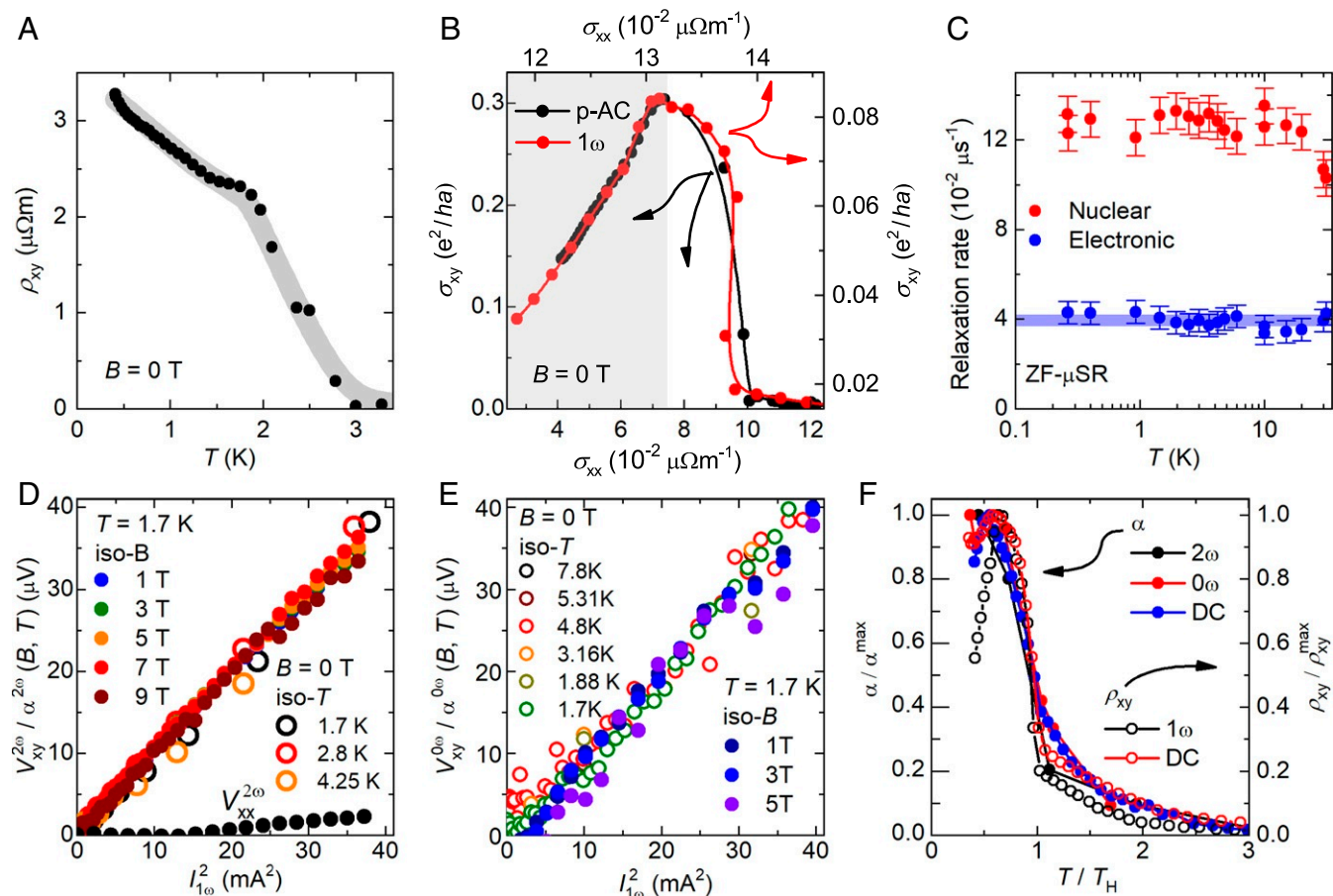


Fig. 2. Spontaneous Hall effect of $\text{Ce}_3\text{Bi}_4\text{Pd}_3$. (A) Temperature-dependent direct current (DC) Hall resistivity ρ_{xy} in zero external magnetic field, showing a pronounced spontaneous Hall effect below 3 K. Data were taken without prior application of magnetic fields. (B) Spontaneous DC Hall conductivity σ_{xy} in units of the 3D conductivity quantum vs. longitudinal conductivity σ_{xx} , with temperature as implicit parameter, for the DC response of the sample in A (bottom and left axes, black) and for the 1ω response in an AC experiment on a sample from a different batch (top and right axes, red), both in zero magnetic field. In the Kondo coherent regime (gray shading), σ_{xy} is linear in σ_{xx} . (C) Temperature-dependent nuclear and electronic contributions to the muon spin relaxation rate obtained from ZF μSR measurements. The electronic contribution is extremely small and temperature-independent within the error bars, ruling out TRS breaking with state-of-the-art accuracy. Magnetization and specific heat measurements corroborate this finding (see *SI Appendix, sections II B and C and Figs. S11 and S12*). (D) Scaled 2ω spontaneous Hall voltage vs. square of 1ω driving electrical current in zero magnetic field for different temperatures and at 1.7 K for various magnetic fields. (E) Quantities analogous to D for the 0ω spontaneous Hall voltage. (F) Scaled coefficients of square-in-current response $\alpha^{2\omega,0\omega,\text{DC}}$ from D and E and *SI Appendix, Fig. S6*, respectively (left axis) and linear-in-current response $\rho_{xy}^{1\omega,\text{DC}}$ from B (right axis), as function of scaled temperature (T_H is the onset temperature of the spontaneous Hall signal). The absolute values of $\alpha^{\text{max},i}$, $\rho_{xy}^{\text{max},i}$, and T_H are listed in *SI Appendix, Table S1*.

linear-in-field behavior consistent with a single hole-like band, strong nonlinearities appear below T^* . Most importantly, a large even-in-field component $\rho_{xy}^{\text{even}} = [\rho_{xy}(B) + \rho_{xy}(-B)]/2$ is observed (Fig. 3C) that even overwhelms the usual odd-in-field component $\rho_{xy}^{\text{odd}} = [\rho_{xy}(B) - \rho_{xy}(-B)]/2$ (Fig. 3E). The nonlinear part of the latter, that scales with $[\rho_{xx} - \rho_{xx}(4\text{K})]^2$ and is thus independent of the scattering time (Fig. 3F), is theoretically expected (35) and experimentally observed (36) in TRS broken Weyl semimetals, which is here realized by the finite magnetic field. The exciting discovery, however, is the even-in- B component, which is the finite-field extension of the spontaneous Hall effect. Both are incompatible with the standard (magnetic field or magnetization induced) Hall conductivity mechanism, where the elements σ_{xy} of the fully antisymmetric Hall conductivity tensor may couple only to a physical quantity G that breaks TRS (i.e., $TG = -G$, where T is the time-reversal operation) (37) and thus have to be an odd function of this quantity [e.g., $\sigma_{xy}(B) = -\sigma_{xy}(-B)$, where $G = B$].

The question, then, is how to understand the Hall response beyond a broken TRS framework. Recent theoretical studies

(38) show that in an IS breaking but TRS preserving material, a Hall current (density)

$$j_y = \sigma_{xy} \mathcal{E}_x = \frac{e^2}{\hbar} \int \frac{d^3k}{(2\pi)^3} f(\mathbf{k}) \underbrace{\Omega_z^{\text{odd}}(\mathbf{k})}_{v_y} \mathcal{E}_x \quad [1]$$

can be generated in a current-carrying state, as nonlinear response to an applied electric field \mathcal{E}_x . This field changes the equilibrium (Fermi-Dirac) distribution function $f_0(\mathbf{k})$ into the nonequilibrium distribution function $f(\mathbf{k})$. In addition, in the presence of the Berry curvature $\Omega_z^{\text{odd}}(\mathbf{k})$, that is odd in \mathbf{k} [i.e., $\Omega_z^{\text{odd}}(\mathbf{k}) = -\Omega_z^{\text{odd}}(-\mathbf{k})$] for systems with broken IS (39), it generates the anomalous velocity v_y . This state breaks TRS at the thermodynamic level, as $f(\mathbf{k})$ can be maintained only at the cost of entropy production ($\dot{S} = j_x \mathcal{E}_x$). The Hall conductivity σ_{xy} in Eq. 1 is finite only under this condition, which is in contrast to a normal (linear-response) Hall conductivity (*SI Appendix, section I E*).

Because σ_{xy} of Eq. 1 is driven by this TRS invariant Berry curvature and not by an applied magnetic field, it does not need

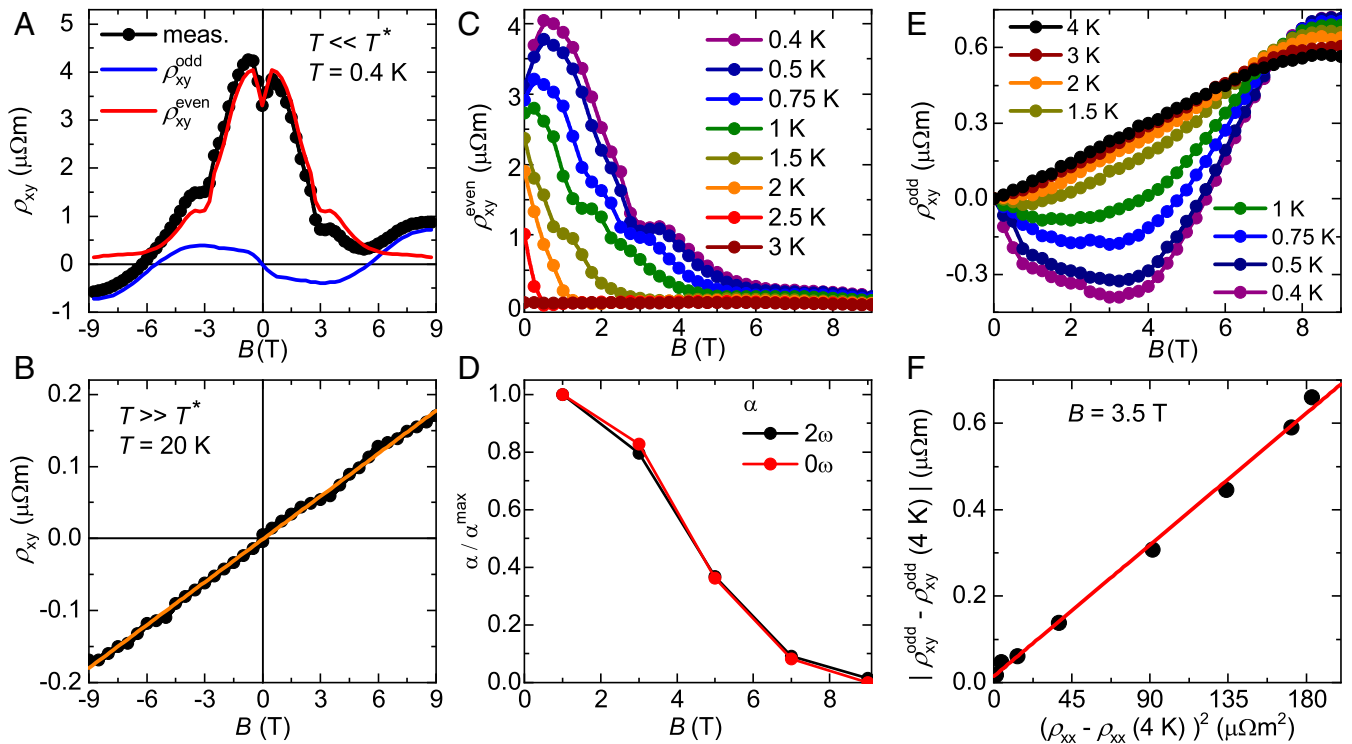


Fig. 3. Hall resistivity of $\text{Ce}_3\text{Bi}_4\text{Pd}_3$ in external magnetic fields. (A) In the Kondo coherent regime below T^* and B_0^* (Fig. 1D), the magnetic field-dependent DC Hall resistivity $\rho_{xy}(B)$ shows a pronounced anomalous Hall effect (AHE) and can be decomposed into an odd-in- B $\rho_{xy}^{\text{odd}}(B)$ (blue) and an even-in- B $\rho_{xy}^{\text{even}}(B)$ (red) component. (B) Above T^* , $\rho_{xy}(B)$ is dominated by a linear-in- B normal Hall effect. (C) $\rho_{xy}^{\text{even}}(B, T)$ is suppressed for $T > T^*$ and $B > B_0^*$. (D) Scaled coefficients of the 2ω and 0ω Hall voltage in an AC experiment (from Fig. 2D and F) as function of magnetic field. (E) Below T^* and B_0^* , $\rho_{xy}^{\text{odd}}(B, T)$ shows a pronounced AHE on top of a linear background from the normal Hall effect. (F) Amplitude of the odd-in- B AHE, estimated as the total odd-in- B component at 3.5 T (location of extremum) minus its value at 4 K, where the effect has disappeared (see E), vs. the square of the corresponding magnetoresistance difference $[\rho_{xx}(T) - \rho_{xx}(4\text{ K})]$ at 3.5 T, with T as implicit parameter. The observed quadratic dependence (red straight line) is in remarkable agreement with expectations for the AHE due to broken TRS as B is applied.

to be odd in B , and a finite σ_{xy} does not even require the presence of any B at all (thus the spontaneous Hall effect). In fact, the only influence the magnetic field has on this topological Hall effect is to successively reduce its magnitude with increasing field (Fig. 3D), similar to what happens when heating the material beyond T^* (Fig. 3C). The observations of a spontaneous Hall effect (Fig. 2) and an even-in-field Hall conductivity (Fig. 3) in $\text{Ce}_3\text{Bi}_4\text{Pd}_3$ are smoking-gun evidence that the physical quantity underlying the phenomenon is not a magnetic order parameter (coupled linearly to B), as otherwise σ_{xy} would necessarily be an odd function in B . That the spontaneous Hall current is indeed associated with $f(\mathbf{k})$ is further supported by the linear relationship between σ_{xy} and σ_{xx} in the Kondo coherent regime (Fig. 2B), consistent with a linear dependence on the scattering time ($\sigma_{xy} \sim \tau$) and thus the nonequilibrium nature of the effect. As recently emphasized (40), this dependence sharply discriminates this effect from disorder-induced contributions.

Because according to Eq. 1 the topological Hall current is determined by $f(\mathbf{k})$, σ_{xy} will depend on \mathcal{E}_x , and thus the Hall response $j_y = \sigma_{xy}(\mathcal{E}_x) \cdot \mathcal{E}_x$ is expected to be nonlinear in \mathcal{E}_x . By Taylor expanding $f(\mathbf{k})$ around $f_0(\mathbf{k})$, a second harmonic response was derived (38), which we have set out to probe by investigating both the dependence of the Hall response on the electric field (or current) strength and by analyzing the different components of the Hall response under AC and DC current drives (SI Appendix, section I D). As we will show in what follows, we do indeed observe this second harmonic response; in addition, however, we also detect terms that go beyond the prediction. The experiments as function of DC current drive reveal that the spontaneous Hall

voltage V_{xy}^{DC} can be decomposed into a linear- and a quadratic-in- I^{DC} contribution (SI Appendix, Fig. S6A, Right). This is in contrast to the longitudinal voltage V_{xx}^{DC} that is linear in current, representing an ohmic electrical resistivity (SI Appendix, Fig. S6A, Left). In our AC experiments, in response to an excitation at frequency ω we detect voltage contributions at 1ω , 2ω , and 0ω . Whereas $V_{xy}^{1\omega}$ is linear in $I^{1\omega}$ (SI Appendix, Fig. S7B), both $V_{xy}^{2\omega}$ and the associated current rectified counterpart $V_{xy}^{0\omega}$ (SI Appendix, Eq. S10) are quadratic in $I^{1\omega}$ (Fig. 2D and E). These three responses as well as the DC response described above appear simultaneously, as Kondo coherence develops with decreasing temperature (Fig. 2F) and must thus have a common origin.

Discussion

We start by discussing the terms $V_{xy}^{2\omega}$, $V_{xy}^{0\omega}$, and $V_{xy}^{\text{DC}} \sim I^2$. They can be understood within the perturbative treatment (38) of Eq. 1, where the spontaneous nonlinear Hall conductivity σ_{xy} is determined by the Berry curvature dipole D_{xz} as

$$\sigma_{xy} = \frac{e^3 \tau}{\hbar^2} \cdot D_{xz} \cdot \mathcal{E}_x \quad \text{with} \quad D_{xz} = \int \frac{d^3 k}{(2\pi)^3} f_0(\mathbf{k}) \frac{\partial \Omega_z^{\text{odd}}}{\partial k_x}. \quad [2]$$

For several noninteracting (and TRS-preserving) Weyl semimetals, D_{xz} was computed by electronic bandstructure calculations (41). The tangent of the Hall angle, defined as $\tan \Theta_{\text{H}} \equiv \sigma_{xy} / \sigma_{xx}$, where σ_{xx} is the normal (1ω) longitudinal conductivity, was found to be at maximum (if the chemical potential is placed at the Weyl nodes) of the order 10^{-4} for a scattering time

$\tau = 10$ ps and an electric field of $\mathcal{E}_x = 10^2$ V/m, corresponding to $\tan \Theta_H / \mathcal{E}_x \leq 10^{-6}$ m/V (41). An experimental confirmation of these predictions remains elusive to date. For $\text{Ce}_3\text{Bi}_4\text{Pd}_3$, we have measured $\tan \Theta_H / \mathcal{E}_x$ values as large as 3×10^{-3} m/V in the second harmonic channel (Fig. 2D). This giant value is even more surprising as it is obtained in a bulk semimetal, without any chemical potential tuning. Experimentally, such tuning is limited to the case of insulating (quasi) two-dimensional materials. Two comments are due. First, in gate-tuned bilayer (42) and few-layer (43) WTe_2 , which both feature a gap at the Fermi level, 2ω Hall voltages have recently been reported; they were attributed to a large—but not divergent—Berry curvature. We estimate the maximum values reached there to be $\tan \Theta_H \approx 5 \times 10^{-3}$ and 10^{-4} and $\tan \Theta_H / \mathcal{E}_x \approx 3 \times 10^{-6}$ m/V and 10^{-8} m/V, respectively, thus again at least three orders of magnitude smaller than what we observe in $\text{Ce}_3\text{Bi}_4\text{Pd}_3$. Second, we point out that the above-discussed spontaneous nonlinear Hall effect is not to be confused with the AHE in TRS breaking Weyl semimetals (36) or the planar Hall effect in noncentrosymmetric Weyl semimetals (44). In the former, the Berry curvature is related to a magnetization. In the latter, the amplitude of the effect is determined by that of the chiral anomaly (44), which is strongly suppressed in Weyl–Kondo semimetals.

Next, we quantify the terms $V_{xy}^{1\omega}$ and $V_{xy}^{\text{DC}} \sim I$ that have not been considered in the perturbative approach of ref (38), though odd-in-current contributions can generally appear (SI Appendix, section I F). Intriguingly, these linear contributions show $\tan \Theta_H$ values up to 0.5 (taken as the slope $\partial \sigma_{xy} / \partial \sigma_{xx}$ in Fig. 2B and SI Appendix, Fig. S8B) and thus are even larger than the 2ω effect quantified above. Before describing how these new terms as well as the above-discussed spontaneous nonlinear Hall terms may naturally arise in a Weyl–Kondo semimetal picture, we show that other effects can be safely discarded.

Skew scattering, side jump, and multiband effects are investigated via the normal (antisymmetrized) Hall effect and magnetoresistance characteristics and shown to play negligible roles by quantitative analyses (SI Appendix, sections I B and C and Figs. S4 and S5). Spurious Hall contributions due to crystal anisotropies, which may arise in systems with lower than cubic symmetry, can also be ruled out (SI Appendix, section I G). Finally, the reproducibility of the spontaneous Hall effect over various samples (SI Appendix, Fig. S8) confirms the intrinsic nature of this phenomenon.

In a Weyl–Kondo semimetal, the Weyl nodes—where the Berry curvature is singular—are essentially pinned to the Fermi level (30, 31). The application of even small electric fields has

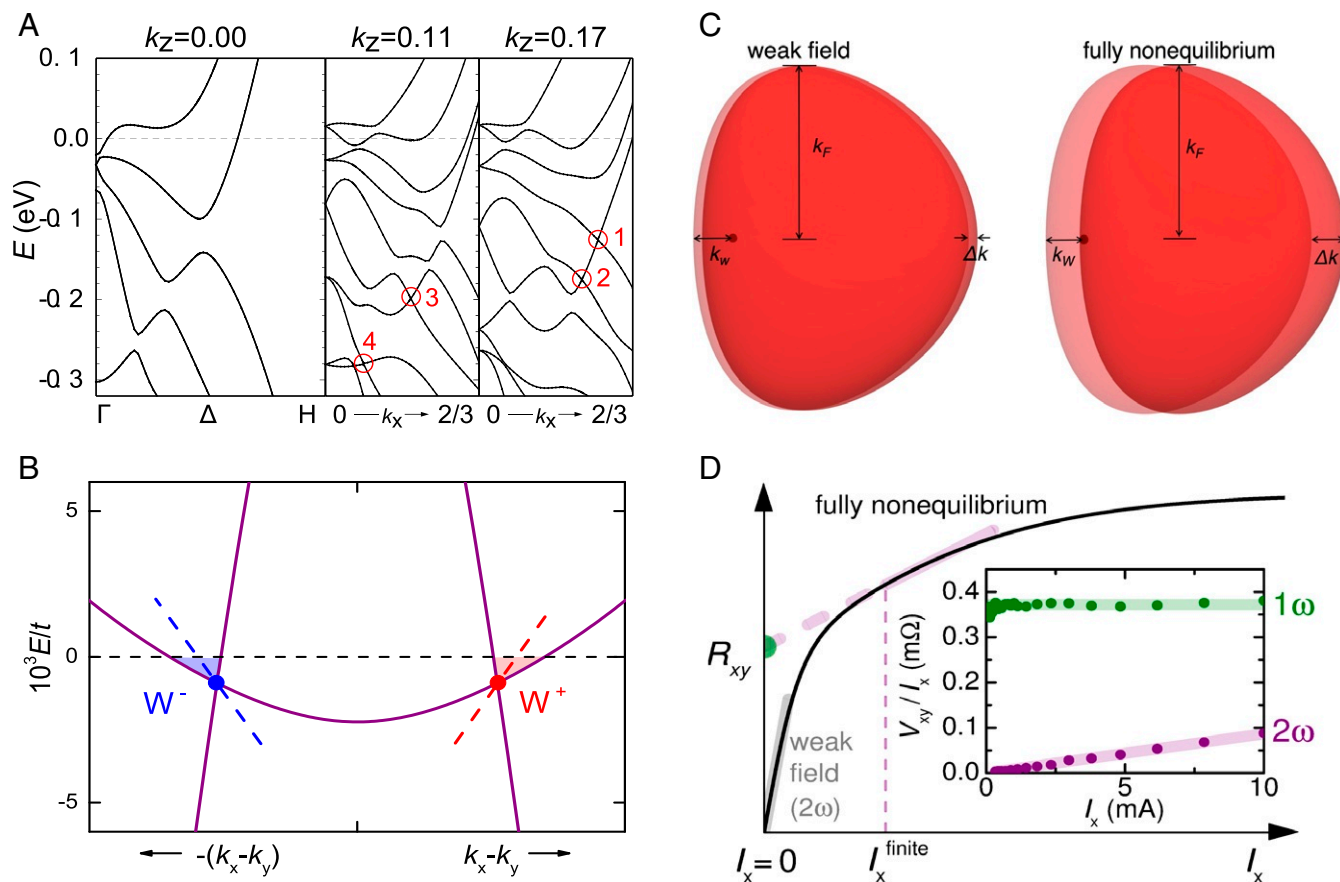


Fig. 4. Theoretical description of Weyl–Kondo physics in $\text{Ce}_3\text{Bi}_4\text{Pd}_3$. (A) Ab initio band structure of $\text{Ce}_3\text{Bi}_4\text{Pd}_3$, with 4f electrons in the core. In the k_x – k_z plane, four different Weyl nodes (1–4) are identified; 1 and 4 are most strongly tilted (SI Appendix, section III). (B) Dispersion across a pair of Weyl (W^+) and anti-Weyl (W^-) nodes for a Weyl–Kondo model with tilted Weyl cones (SI Appendix, section IV). Energy is expressed in units of the conduction electron bandwidth t . The Kondo interaction pushes the Weyl nodes that are present in the bare conduction electron band far away from the Fermi energy, to the immediate vicinity of the Fermi level (here at $E/t = 0$, slightly above the Weyl nodes). (C) Sketch of a Fermi pocket around the Weyl node W^+ in B (dot) in zero electric field (light red) and its nonequilibrium counterpart with driving electric field (red), in the weak-field regime (left) and the fully nonequilibrium regime (right). (D) Sketch of the driving current-induced Hall resistance $R_{xy} = V_{xy}/I_x$, displaying the weak-field and fully nonequilibrium regimes. The Inset shows experimental results for $\text{Ce}_3\text{Bi}_4\text{Pd}_3$, demonstrating the simultaneous presence of a spontaneous Hall signal in both the 2ω ($V_{xy} \sim I_x^2$) and 1ω ($V_{xy} \sim I_x$) channel. The sum of both contributions corresponds to a linear-in- I_x Hall resistance with a finite offset (violet line with green dot in main panel), which is a characteristic of the fully nonequilibrium regime.

a nonperturbative effect, in particular in the case of tilted Weyl cones (see *SI Appendix, section IV C* for an expanded discussion). A simple Taylor expansion of $f(\mathbf{k})$ around $f_0(\mathbf{k})$, as done in ref. 38, will therefore fail to describe the effect. Quantitative predictions from fully nonequilibrium transport calculations based on an *ab initio* electronic bandstructure in the limit of strong Coulomb interaction and strong spin-orbit coupling are elusive to date. Thus, instead, we here present a conceptual understanding. While tilted Weyl cones are present already in the noninteracting bandstructure of $\text{Ce}_3\text{Bi}_4\text{Pd}_3$ (Fig. 4A and *SI Appendix, section III*), it is the Kondo interaction that drives emergent and highly renormalized Weyl nodes in the immediate vicinity of the Fermi level (Fig. 4B), as indicated by calculations for a periodic Anderson model (31) with tilted Weyl cones in the bare conduction electron band (*SI Appendix, section IV and Fig. S13*) and evidenced by thermodynamic measurements (30). In the resulting tilted Weyl-Kondo semimetal, each Weyl node will be asymmetrically surrounded by a small Fermi pocket. The presence of such small pockets in $\text{Ce}_3\text{Bi}_4\text{Pd}_3$ is supported by the small carrier concentration ($8 \times 10^{19} \text{ cm}^{-3}$, or 0.002 charge carriers per atom) obtained from the normal Hall coefficient (*SI Appendix, Fig. S4A*). Due to the pinning of the Fermi energy to the Weyl nodes in a tilted Weyl-Kondo semimetal, the smallest distance between node and Fermi surface (k_{W} , see Fig. 4C) can become extremely small. The application of even tiny electric fields will then induce shifts Δk in the distribution function $f(\mathbf{k})$ that are sizable compared to k_{W} (and possibly even compared to the Fermi wavevector k_{F}), thus driving the system to a fully nonequilibrium regime (Fig. 4D). In this setting, a nonperturbative approach is needed and will allow for the appearance of terms beyond the second harmonic one predicted by Sodemann and Fu (38), most notably the experimentally observed first harmonic one (*SI Appendix, section I D*). As the applied \mathcal{E} field can then no longer be considered as a probing field, it introduces a directionality on top of the crystal's space group symmetry and the selection rules, which hold in the perturbative regime, will be violated.

In conclusion, our Hall effect measurements unambiguously identify a giant Berry curvature contribution in a time-reversal invariant material, the noncentrosymmetric heavy fermion semimetal $\text{Ce}_3\text{Bi}_4\text{Pd}_3$. The Hall angle per applied electric field, a figure of merit of the effect, is enhanced by orders of magnitude over values expected for weakly interacting systems, which we attribute to the effect of tilted and highly renormalized Weyl nodes that emerge very close to the Fermi surface out of the Kondo effect. The experiments reported here should allow for a ready identification of other strongly correlated nonmagnetic Weyl semimetals, be it in heavy fermion compounds or in other materials classes, thereby enabling much needed systematic studies of the interplay between strong correlations and topology. Our findings provide a window into the landscape of “extreme topological matter”—where strong correlations lead to extreme topological responses—that awaits systematic exploration. Finally, the discovered effect being present in a 3D material, in the absence of any magnetic fields and under only tiny driving electric fields, holds great promise for the development of robust topological quantum devices.

Materials and Methods

Synthesis. Single crystals of $\text{Ce}_3\text{Bi}_4\text{Pd}_3$ and the nonmagnetic reference compound $\text{La}_3\text{Bi}_4\text{Pd}_3$ were synthesized using a Bi-flux method (30). Their stoichiometry, phase purity, crystal structure, and single crystallinity were verified using powder X-ray diffraction, scanning electron microscopy (SEM), energy dispersive X-ray spectroscopy (EDX), and Laue diffraction. Because $\text{Ce}_3\text{Bi}_4\text{Pd}_3$ is a stoichiometric compound in which all three elements have unique crystallographic sites, disorder is expected to be weak.

Measurement Setups. Magnetotransport measurements were performed using various devices: two Quantum Design Physical Property Measurement Systems, in part with ^3He or vertical rotator option, and an Oxford ^4He flow cryostat using a Stanford Research SR830 lock-in amplifier. In the former, we used a pseudo-AC technique and in the latter a standard AC technique with lock-in detection. Electrical contacts for these measurements were made by spot-welding 12- μm -diameter gold wires to the samples in a five- or six-wire configuration, depending on the crystal size. Oriented single crystals were studied with the driving electrical current along different crystallographic directions (approximately along [103], [111], and [100]).

The μSR measurements were performed at the Dolly spectrometer of the Swiss Muon Source at Paul Scherrer Institut, Villigen. The single crystals were aligned to form a mosaic with about 1-cm diameter and a thickness of about 0.5 mm, glued on top of a thin copper foil solidly clamped to a copper frame, thus optimally using the muon beam cross-section, minimizing the background from the sample holder, and guaranteeing good thermal contact. Combined with active vetoing, this setup resulted in very low spurious background signals. A cold-finger Oxford Heliox ^3He system combined with a ^4He Oxford Variox cryostat was used to reach temperatures down to 250 mK. By employing active compensation coils, true ZF conditions could be achieved during the ZF μSR experiments.

Ab Initio Calculations. We performed non-spin-polarized band structure calculations for $\text{Ce}_3\text{Bi}_4\text{Pd}_3$ based on density functional theory, treating the Ce $4f$ electrons in the open-core approximation and taking spin-orbit interaction into account. Weyl nodes in the k_x - k_z plane of the Brillouin zone were identified via their Berry curvature (see *SI Appendix, section III* for further details).

Model Calculations. We extended the model for a Weyl-Kondo semimetal (31) to include beyond nearest-neighbor hopping terms and solved the self-consistent saddle-point equations for the strong interaction limit of the periodic Anderson model. We find a Weyl-Kondo solution with tilted Weyl cones. With the Kondo interaction placing the Fermi energy very close to the Weyl nodes, the Fermi surface comprises Fermi pockets that are asymmetrically distributed near the Weyl and anti-Weyl nodes. The Berry curvature, which diverges exactly at any Weyl or anti-Weyl node, is thus very large on the Fermi surface (see *SI Appendix, section IV* for further details).

Data Availability. All study data are included in the article and/or *SI Appendix*.

ACKNOWLEDGMENTS. We thank J.-C. Orain for technical assistance during the μSR experiments, C. Wilhelmer for contributions to transport experiments, R. Svagera and M. Waas for SEM-EDX investigations, and J. Mesot and D. A. Zocco for fruitful discussion. The team in Vienna acknowledges financial support from the Austrian Science Fund (FWF Grants P29279-N27, P29296-N27, and DK W1243) and the European Union's Horizon 2020 Research and Innovation Program, under Grant Agreement EMP-824109. T.S. acknowledges support from the Swiss National Science Foundation (SNF Grant 200021-169455). Work at Rice was in part supported by the NSF (DMR-1920740) and the Robert A. Welch Foundation (C-1411) and by a Ulam Scholarship from the Center for Nonlinear Studies at Los Alamos National Laboratory. Q.S. and S.P. acknowledge the hospitality of the Aspen Center for Physics, which is supported by the NSF Grant PHY-1607611.

1. Topology on top. *Nat. Phys.* **12**, 615 (2016).
2. M. Asorey, Space, matter and topology. *Nat. Phys.* **12**, 616–618 (2016).
3. C. Beenakker, L. Kouwenhoven, A road to reality with topological superconductors. *Nat. Phys.* **12**, 618–621 (2016).
4. S. D. Huber, Topological mechanics. *Nat. Phys.* **12**, 621–623 (2016).
5. Y. E. Kraus, O. Zeitlinger, Quasiperiodicity and topology transcend dimensions. *Nat. Phys.* **12**, 624–626 (2016).
6. L. Lu, J. D. Joannopoulos, M. Soljačić, Topological states in photonic systems. *Nat. Phys.* **12**, 626–629 (2016).
7. N. Goldman, J. C. Budich, P. Zoller, Topological quantum matter with ultracold gases in optical lattices. *Nat. Phys.* **12**, 639–645 (2016).

8. M. König *et al.*, Quantum spin Hall insulator state in HgTe quantum wells. *Science* **318**, 766–770 (2007).
9. D. Hsieh *et al.*, A tunable topological insulator in the spin helical Dirac transport regime. *Nature* **460**, 1101–1105 (2009).
10. S. Sasaki *et al.*, Topological superconductivity in $\text{Cu}_x\text{Bi}_2\text{Se}_3$. *Phys. Rev. Lett.* **107**, 217001 (2011).
11. L. Wu *et al.*, Giant anisotropic nonlinear optical response in transition metal monopnictide Weyl semimetals. *Nat. Phys.* **13**, 350–355 (2016).
12. Q. Ma *et al.*, Direct optical detection of Weyl fermion chirality in a topological semimetal. *Nat. Phys.* **13**, 842–847 (2017).

13. N. P. Armitage, E. J. Mele, A. Vishwanath, Weyl and Dirac semimetals in three-dimensional solids. *Rev. Mod. Phys.* **90**, 015001 (2018).
14. S.-M. Huang *et al.*, A Weyl fermion semimetal with surface Fermi arcs in the transition metal monopnictide TaAs class. *Nat. Commun.* **6**, 7373 (2015).
15. S.-Y. Xu *et al.*, Discovery of a Weyl fermion semimetal and topological Fermi arcs. *Science* **349**, 613–617 (2015).
16. N. Xu *et al.*, Observation of Weyl nodes and Fermi arcs in tantalum phosphide. *Nat. Commun.* **7**, 11006 (2016).
17. X. Huang *et al.*, Observation of the chiral-anomaly-induced negative magnetoresistance in 3D Weyl semimetal TaAs. *Phys. Rev. X* **5**, 031023 (2015).
18. C.-L. Zhang *et al.*, Signatures of the Adler–Bell–Jackiw chiral anomaly in a Weyl fermion semimetal. *Nat. Commun.* **7**, 10735 (2016).
19. P. J. W. Moll *et al.*, Transport evidence for Fermi-arc-mediated chirality transfer in the Dirac semimetal Cd₃As₂. *Nature* **535**, 266–270 (2016).
20. C. Zhang *et al.*, Quantum Hall effect based on Weyl orbits in Cd₃As₂. *Nature* **565**, 331–336 (2019).
21. S. Han, C. Lee, E.-G. Moon, H. Min, Emergent anisotropic non-Fermi liquid at a topological phase transition in three dimensions. *Phys. Rev. Lett.* **122**, 187601 (2019).
22. T. Meng, J. C. Budich, Unpaired Weyl nodes from long-ranged interactions: Fate of quantum anomalies. *Phys. Rev. Lett.* **122**, 046402 (2019).
23. M. Kang *et al.*, Dirac fermions and flat bands in the ideal kagome metal FeSn. *Nat. Mater.* **19**, 163–169 (2020).
24. Y. Shao *et al.*, Electronic correlations in nodal-line semimetals. *Nat. Phys.* **16**, 636–641 (2020).
25. B.-J. Yang, E.-G. Moon, H. Isobe, N. Nagaosa, Quantum criticality of topological phase transitions in three-dimensional interacting electronic systems. *Nat. Phys.* **10**, 774–778 (2014).
26. W. K. Park *et al.*, Topological surface states interacting with bulk excitations in the Kondo insulator SmB₆ revealed via planar tunneling spectroscopy. *Proc. Natl. Acad. Sci. U.S.A.* **113**, 6599–6604 (2016).
27. D. Castelvecchi, The shape of things to come. *Nature* **547**, 272 (2017).
28. M. Ippoliti, R. N. Bhatt, F. D. M. Haldane, Geometry of flux attachment in anisotropic fractional quantum Hall states. *Phys. Rev. B* **98**, 085101 (2018).
29. A. Rahmani, M. Franz, Interacting Majorana fermions. *Rep. Prog. Phys.* **82**, 084501 (2019).
30. S. Dzsaber *et al.*, Kondo insulator to semimetal transformation tuned by spin-orbit coupling. *Phys. Rev. Lett.* **118**, 246601 (2017).
31. H.-H. Lai, S. E. Grefe, S. Paschen, Q. Si, Weyl-Kondo semimetal in heavy-fermion systems. *Proc. Natl. Acad. Sci. U.S.A.* **115**, 93 (2018).
32. P. Schlottmann, Bethe-Ansatz solution of the ground-state of the SU(2j + 1) Kondo (Coqblin-Schrieffer) model: Magnetization, magnetoresistance and universality. *Z. Phys. B* **51**, 223–235 (1983).
33. Y. P. Singh *et al.*, From local moment to mixed-valence regime in Ce_{1-x}Yb_xCoIn₅ alloys. *Phys. Rev. B* **89**, 115106 (2014).
34. M. B. Maple *et al.*, Field-dependent ordered phases and Kondo phenomena in the filled skutterudite compound PrOs₄As₁₂. *Proc. Natl. Acad. Sci. U.S.A.* **103**, 6783–6789 (2006).
35. N. Nagaosa, J. Sinova, S. Onoda, A. H. MacDonald, N. P. Ong, Anomalous Hall effect. *Rev. Mod. Phys.* **82**, 1539–1592 (2010).
36. E. Liu *et al.*, Giant anomalous Hall effect in a ferromagnetic kagome-lattice semimetal. *Nat. Phys.* **14**, 1125–1131 (2018).
37. H. B. G. Casimir, On Onsager's principle of microscopic reversibility. *Rev. Mod. Phys.* **17**, 343–350 (1945).
38. I. Sodemann, L. Fu, Quantum nonlinear Hall effect induced by Berry curvature dipole in time-reversal invariant materials. *Phys. Rev. Lett.* **115**, 216806 (2015).
39. D. Xiao, M.-C. Chang, Q. Niu, Berry phase effects on electronic properties. *Rev. Mod. Phys.* **82**, 1959–2007 (2010).
40. Z. Z. Du, C. M. Wang, S. Li, H.-Z. Lu, X. C. Xie, Disorder-induced nonlinear Hall effect with time-reversal symmetry. *Nat. Commun.* **10**, 3047 (2019).
41. Y. Zhang, Y. Sun, B. Yan, Berry curvature dipole in Weyl semimetal materials: An *ab initio* study. *Phys. Rev. B* **97**, 041101 (2018).
42. Q. Ma *et al.*, Observation of the nonlinear Hall effect under time-reversal-symmetric conditions. *Nature* **565**, 337–342 (2019).
43. K. Kang, T. Li, E. Sohn, J. Shan, K. F. Mak, Nonlinear anomalous Hall effect in few-layer WTe₂. *Nat. Mater.* **18**, 324–328 (2019).
44. S. Nandy, G. Sharma, A. Taraphder, S. Tewari, Chiral anomaly as the origin of the planar Hall effect in Weyl semimetals. *Phys. Rev. Lett.* **119**, 176804 (2017).

Supplementary Information for

Giant spontaneous Hall effect in a nonmagnetic Weyl-Kondo semimetal

S. Dzsaber, X. Yan, M. Taupin, G. Eguchi, A. Prokofiev, T. Shiroka, P. Blaha, O. Rubel, S. E. Grefe, H.-H. Lai, Q. Si, and S. Paschen

Corresponding Author: Silke Paschen

Email: paschen@ifp.tuwien.ac.at

This PDF file includes:

Supplementary Text Sects. I to IV

Figures S1 to S15

Tables S1 and S2

Equations S1 to S36

SI References

Supplementary Text

I. ANALYSIS OF HALL EFFECT AND RESISTIVITY DATA

A. Magnetotransport measurement geometry

We define the electrical current direction as x . The electrical resistivity along this direction is thus denoted by ρ_{xx} . A magnetic field applied along x leads to longitudinal magnetoresistance, a field perpendicular to x to transverse magnetoresistance. To detect a normal Hall response, a magnetic field is applied along z , and an electric field along y is measured via voltage contacts perpendicular to x and z .

However, in practice, by contacting the (small) samples with the spot welding technique (Methods), this geometry cannot be perfectly achieved, leading to misalignment contributions for both the resistance and the Hall effect measurements (Fig. S1). We start by discussing the latter. We denote the resistance measured across imperfectly aligned Hall contacts as R_{xy}^{meas} , the genuine Hall resistance as R_{xy} . The established technique to cancel out misalignment contributions in the normal Hall effect is to measure R_{xy}^{meas} for positive and negative magnetic fields and antisymmetrize the signal as

$$R_{xy} = \frac{R_{xy}^{\text{meas}}(+B_z) - R_{xy}^{\text{meas}}(-B_z)}{2} . \quad (\text{S1})$$

For the spontaneous and even-in-field Hall response, however, a different approach is needed.

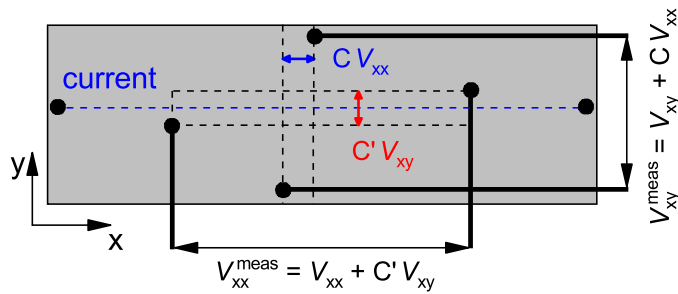


FIG. S1: **Misalignment contributions due to imperfect contact geometry.** Because of unavoidable contact misalignment, the measured voltages across the (longitudinal) resistivity and Hall contacts (V_{xx}^{meas} and V_{xy}^{meas}) contain, in addition to the intrinsic contributions V_{xx} and V_{xy} , the misalignment contributions $C'V_{xy}$ and CV_{xx} , respectively.

At room temperature and in zero applied magnetic field, where no Hall response exists, we determine the ratio of resistances measured across the (longitudinal) resistivity and Hall contacts as

$$C = \frac{R_{xy}^{\text{meas}}}{R_{xx}^{\text{meas}}} = \frac{C R_{xx}}{R_{xx}} = 0.553 . \quad (\text{S2})$$

As the misalignment factor C is a purely geometrical quantity and is thus temperature and field independent, the genuine Hall response at arbitrary fields and temperatures is

$$R_{xy}(T, B) = R_{xy}^{\text{meas}}(T, B) - C R_{xx}(T, B) . \quad (\text{S3})$$

In fact, in the correction term we use $R_{xx}^{\text{meas}}(T, B)$ instead of $R_{xx}(T, B)$, thus correcting the effect only to first order. As higher order terms involving the product CC' are very small (for C' see Fig. S3), this is deemed sufficiently accurate. $R_{xy}(T, B = 0)$ is zero from room temperature down to 3 K (Fig. S2), thus ruling out that the additional signal measured across the Hall contacts below 3 K is due to Hall contact misalignment.

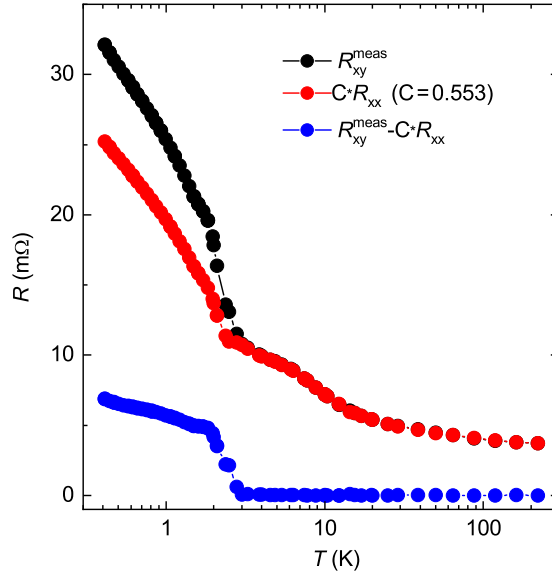


FIG. S2: **Determination of misalignment contribution in DC Hall measurements on $\text{Ce}_3\text{Bi}_4\text{Pd}_3$.** Temperature-dependent electrical resistance measured across the Hall contacts R_{xy}^{meas} (black), longitudinal resistance R_{xx} scaled to R_{xy}^{meas} at room temperature (red), and the difference of the two, $R_{xy} = R_{xy}^{\text{meas}} - C \cdot R_{xx}$ with $C = 0.553$ (blue), all in zero applied magnetic field. A deviation appears only below $T = 3$ K, where the intrinsic spontaneous Hall response sets in. The same procedure is adopted for the 1ω signal of the AC Hall measurements.

This Hall contact misalignment correction is adopted for both the DC transport measurements and the 1ω signal in the AC measurements. As there is no longitudinal signal in the 0ω and 2ω channels, no correction is done for these.

We now turn to the electrical resistivity. Here, the transverse direction misalignment of the contacts leads to the appearance of an additional resistance $C'R_{xy}$, that adds to the intrinsic longitudinal resistance R_{xx} , so that the total measured resistance is $R_{xx}^{\text{meas}} = R_{xx} + C'R_{xy}$ (with R_{xy} obtained via Eqn. S3). We determine the misalignment factor C' as follows: At a temperature above the onset of the spontaneous Hall effect we measure, on the resistivity contacts, the normal Hall resistance $[R_{xx}^{\text{meas}}(+B) - R_{xx}^{\text{meas}}(-B)]/2$ as function of magnetic field (Fig. S3A, black data points). At the same temperature, we also measure the Hall resistance on the Hall contacts, and scale it (by the factor C') such that it collapses onto the former curve (Fig. S3A, red data points). With C' determined in this way, the temperature dependences of $C'R_{xy}$ and thus of R_{xx} can be determined in zero magnetic field, across the onset of spontaneous Hall effect (Fig. S3B). One sees that, with this correction (red curve), the feature in $R_{xx}(T)$ seen at the onset of the spontaneous

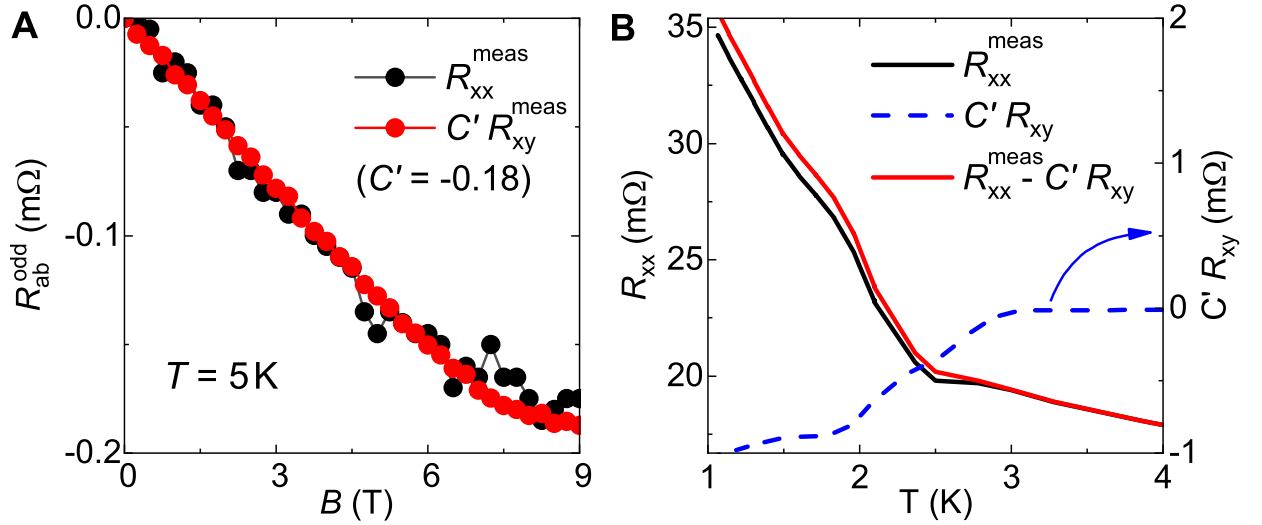


FIG. S3: **Misalignment correction of the electrical resistance.** (A) Measured odd-in- B resistance $R_{ab}^{\text{odd}} = [R_{ab}^{\text{meas}}(+B) - R_{ab}^{\text{meas}}(-B)]/2$ on the electrical resistance contacts ($ab = xx$, black), together with that measured across the Hall contacts and scaled by C' ($ab = xy$, red).

Data are plotted for sample S1 (see MS), and obtained at $T = 5\text{ K}$, above the onset of the spontaneous Hall effect. C' is chosen to achieve best overlap of the curves. (B) With C' obtained from (A), the measured temperature dependent resistance R_{xx}^{meas} (black) is corrected for the misalignment contribution $C'R_{xy}$ (blue dashed line), to obtain the intrinsic curve (red).

Hall effect is weakened, but still visible (see Fig. S9A). The same is true for the other samples studied in this work (Fig. S9B, C). The origin of this additional effect, which is an intrinsic imprint of the Hall conductivity via the giant Hall angle of $\text{Ce}_3\text{Bi}_4\text{Pd}_3$, is discussed in Sect. IH.

Finally, if we do this same correction for the 2ω longitudinal voltage signal $V_{xx}^{2\omega}$, we find that the signal essentially cancels (Fig. 2D). This is because there is no 2ω signal in the (longitudinal) resistance.

B. Skew-scattering and side-jump contributions to the Hall effect

In heavy fermion metals, the Kondo interaction may lead to non-negligible skew scattering [29, 39–42]. The (linear-response) Hall coefficient in the Kondo incoherent regime then reads

$$R_H(T) = R_H^0 + C_1 \rho_{\text{mag}}(T) \chi(T) , \quad (\text{S4})$$

where R_H^0 is the normal Hall coefficient due to charge carriers [in a simple single-band metal with a temperature-independent charge carrier concentration n , $R_H^0 = 1/(ne)$], ρ_{mag} is the magnetic contribution to the electrical resistivity (defined as $\rho_{\text{mag}} = \rho_{xx}^{\text{Ce}} - \rho_{xx}^{\text{La}}$, where ρ_{xx}^{Ce} and ρ_{xx}^{La} are the resistivity of the Ce-based heavy fermion compound and its nonmagnetic La-based reference compound, respectively), χ is the magnetic susceptibility, and C_1 is a temperature-independent constant.

The linear-response normal Hall coefficient R_H of $\text{Ce}_3\text{Bi}_4\text{Pd}_3$ is obtained from the total anti-symmetrized Hall signal (Eqn. S1) at high temperatures, and as $\rho_{xy}^{\text{odd}}(8\text{ T})/(8\text{ T})$ at 4 K and below (see Fig. 3E of the main part). It shows significant temperature dependence at high temperatures, but tends to saturate at low temperatures (Fig. S4A), in agreement with data above 2 K from ref [43], which is typical of a Kondo semimetal. Nevertheless, we here explore whether skew scattering might alternatively lead to this temperature dependence. For this purpose, we plot R_H vs. $\rho_{\text{mag}} \chi^* = \rho_{\text{mag}} \chi / C$, with temperature as an implicit parameter (Fig. S4B), where $C = n_{\text{Ce}} \mu_{\text{eff}}^2 / (3k_B)$ is the Curie constant (n_{Ce} is the concentration and $\mu_{\text{eff}} = 2.54\mu_B$ the effective moment of the Ce^{3+} ions, k_B is the Boltzmann constant). In the fully incoherent regime above 10 K, a linear relationship with the slope $C_1 = 0.38\text{ K/T}$ is indeed observed (Fig. S4B). At first, this seems to suggest that the Hall response of this material is dominated by skew scattering. However, as outlined in what follows, the obtained value of C_1 is unphysically large, indicating that $R_H(T)$ is dominated by the temperature dependence of the charge carrier concentration and not by

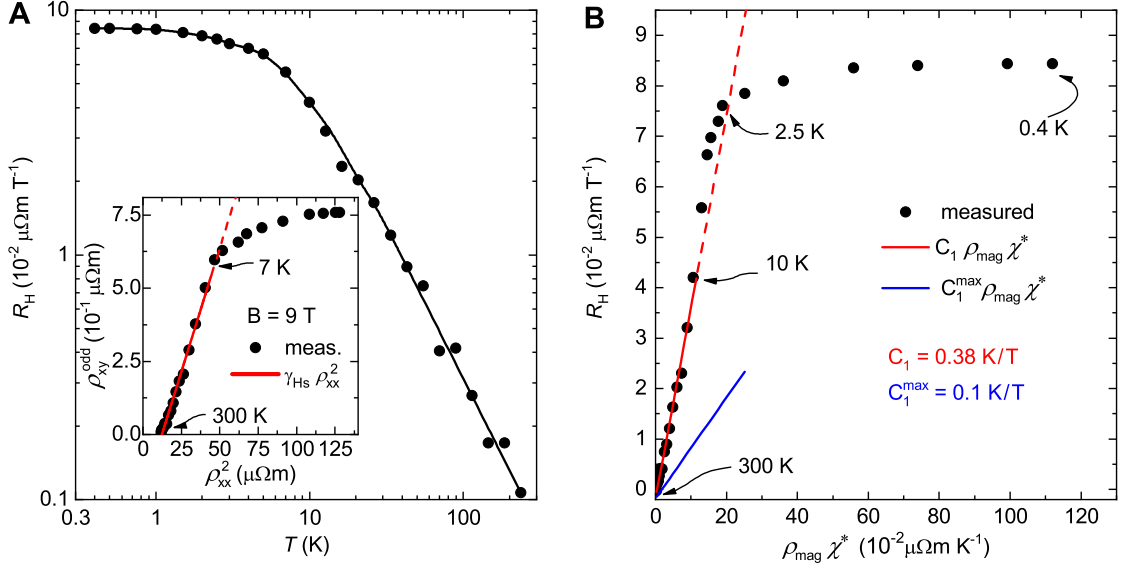


FIG. S4: **Skew scattering and side-jump effect vs. normal Hall effect in $\text{Ce}_3\text{Bi}_4\text{Pd}_3$.** (A) The linear-response normal Hall coefficient R_H of $\text{Ce}_3\text{Bi}_4\text{Pd}_3$ shows pronounced temperature dependence in the incoherent regime. The inset shows the corresponding ρ_{xy}^{odd} vs. ρ_{xx}^2 data. The red line indicates a linear fit between 300 and 7 K with the slope $\gamma_{\text{Hs}} = 0.017 \Omega^{-1} \mu\text{m}^{-1}$. This value is too large to be attributed to the side-jump effect (see text). (B) R_H vs. $\rho_{\text{mag}} \chi^*$, with T as implicit parameter (see text), is linear above 10 K (full red line is a linear fit to the data, red dashed line its extrapolation), but the slope C_1 is too large for this behavior to be attributed to skew scattering (slope of blue line corresponds to the upper boundary).

skew scattering.

For Kondo systems the skew scattering amplitude C_1 is given by[39]

$$C_1 = -\frac{5}{7} g J \frac{\mu_B}{k_B} \cos(\delta) \sin(\delta) \quad \text{with} \quad Z = \frac{2}{\pi} \sum_{-l}^l (2l+1) \delta, \quad (\text{S5})$$

where δ is the phase shift of the Fermi wavefunction due to Kondo scattering, that is related to the valence difference Z between the impurity and the host metal via Friedel's sum rule, l is the orbital quantum number, and J is the quantum number of the spin-orbit coupled total moment. Thus, both δ and C_1 have an upper boundaries. For Ce^{3+} Kondo scatterers ($Z = 1$, $l = 3$), the maximum value $C_1 = 0.1 \text{ K/T}$ (blue line in Fig. S4B) is obtained by assuming full screening of the $4f$ moment ($\delta = \pi/14$). Whereas experimentally determined C_1 values for prototypical heavy fermion metals (e.g., $C_1 = 0.082, 0.075, 0.016,$ and 0.01 K/T for $\text{CeCu}_6, \text{CeAl}_3, \text{CeCoRh}_5,$ and CeCoIr_5 , respectively[39, 40]) are indeed much smaller than this upper boundary, our C_1 value

for $\text{Ce}_3\text{Bi}_4\text{Pd}_3$ strongly overshoots it. In fact, such a large C_1 value is not only incompatible with the Ce^{3+} case, but inconsistent with Eqn. S5 for any phase shift δ , as $|C_1| \leq 0.21$. We therefore conclude that skew scattering plays at best a minor role in determining $R_{\text{H}}(T)$ in the incoherent regime.

In the Kondo coherent regime, skew scattering is known to freeze out with decreasing temperature, any remnant skew scattering amplitude keeping a positive sign in Ce-based heavy fermion compounds [39]. As the anomalous Hall effect we observe in $\text{Ce}_3\text{Bi}_4\text{Pd}_3$ (see Fig. 3E of the main part) increases in magnitude with decreasing temperature and is negative in sign, we can safely discard any influence of skew scattering also here.

An anomalous Hall effect contribution due to the side-jump effect may occur in solids with broken TRS, and is well-known in ferromagnetic phases [29]. As such it cannot account for the spontaneous Hall resistivity we observe (Fig. 2 A). Here we show that, in addition, this mechanism does not play any appreciable role in the finite-field Hall response of $\text{Ce}_3\text{Bi}_4\text{Pd}_3$. The side-jump contribution ρ_{xy}^{Hs} to the Hall resistivity is proportional to τ^0 and thus reads [29, 44]

$$\rho_{xy}^{\text{Hs}} = \gamma_{\text{Hs}} \rho_{xx}^2, \quad (\text{S6})$$

with

$$\gamma_{\text{Hs}} = \frac{ne^2 \Delta y}{\hbar k_{\text{F}}}. \quad (\text{S7})$$

Here $\Delta y \approx 10^{-11}$ m is the amplitude of the side jump in the Hall direction after an impurity scattering event [29, 44], n the carrier concentration, e the electron charge, and k_{F} the Fermi wave vector. For $\text{Ce}_3\text{Bi}_4\text{Pd}_3$, the carrier concentration at 300 mK is $n = 8 \cdot 10^{25} \text{ m}^{-3}$, and we estimate k_{F} (in a simple parabolic, free-electron single-band model) as $k_{\text{F}} = 1.3 \cdot 10^9 \text{ m}^{-1}$, thus yielding the (hypothetical) value $\gamma_{\text{Hs}} = 1.5 \cdot 10^{-4} \Omega^{-1} \mu\text{m}^{-1}$. We do observe the dependence of Eqn. S6 in the Kondo incoherent regime above 7 K (Fig. S4 inset), but with a slope $\gamma_{\text{Hs}} = 1.7 \cdot 10^{-2} \Omega^{-1} \mu\text{m}^{-1}$ that is two orders of magnitude larger than the expectation, making it very unlikely that this dependence is due to the side-jump effect. In the Kondo coherent regime below 7 K, ρ_{xy}^{odd} saturates (Fig. S4 inset) and, thus, side-jump effects are unimportant also there.

Ignoring the above reasoning that side jumps cannot generate a spontaneous Hall contribution, we nevertheless estimate the (non-spontaneous) tangent of the Hall angle due to the side-jump effect. With Eqn. S6 we obtain $\tan \Theta_{\text{H}} = \rho_{xy}^{\text{Hs}} / \rho_{xx} = \gamma_{\text{Hs}} \rho_{xx}$. Using the above estimate of γ_{Hs} and the electrical resistivity $\rho_{xx} \approx 20 \Omega \mu\text{m}$ (Fig. 1 A) yields $\tan \Theta_{\text{H}} \approx 3 \cdot 10^{-3}$, which is three orders of

magnitude smaller than the giant measured value of $\tan \Theta_H \approx 0.5$, confirming that the side-jump effect does not play any appreciable role in $\text{Ce}_3\text{Bi}_4\text{Pd}_3$.

Finally, setting the above quantitative considerations aside, there is a fundamental reason why extrinsic contributions should be ruled out to generate the spontaneous Hall response we observe: The measured $\rho_{xy}(B = 0)$ is zero above the Kondo coherence temperature T^* but impurity scattering should be present at all temperatures.

C. Hall effect from multiple bands

A nonlinear (transverse) magnetoresistance and (odd-in-field) Hall resistivity, as observed for $\text{Ce}_3\text{Bi}_4\text{Pd}_3$ at low temperatures (see Figs. 1E and 3E of the main part, respectively) might, *a priori*, also result from multiple electronic bands contributing to the Fermi surface. In the typically considered two-band case, a key requirement for strong magnetotransport nonlinearities is a large difference in the carrier concentration and mobility of the two bands (e.g., low-mobility majority carriers and high-mobility minority carriers). To examine whether the experimentally observed

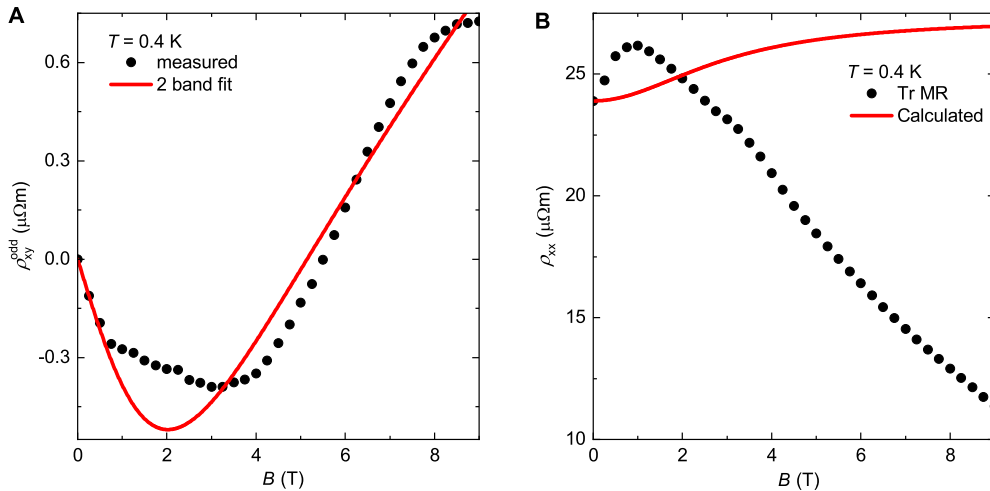


FIG. S5: **Two-band analysis of magnetotransport data of $\text{Ce}_3\text{Bi}_4\text{Pd}_3$.** (A) Odd-in-field Hall resistivity at 0.4 K (from Fig. 3E of the main part) with best fit of a two-band Drude model (red line, see text). (B) Transverse magnetoresistivity at 0.4 K with corresponding curve calculated from the parameters obtained in (A), showing that a two-band model cannot account for the experimental curves.

dependences, attributed to the odd-in-field anomalous Hall effect (Fig. 3E of the main part), might alternatively be produced by two-band effects, we performed a two-band analysis using a recently established robust analysis scheme [45].

We use the $\rho_{xy}^{\text{odd}}(B)$ data at the lowest temperature of 0.4 K (Fig. 3E of the main part), where the nonlinearity is largest. Though the obtained best fit cannot fully account for the field dependence, it reproduces the overall shape of $\rho_{xy}^{\text{odd}}(B)$ (Fig. S5A). The obtained charge carrier concentrations and mobilities are $n_1 = 3.39 \times 10^{19} \text{ cm}^{-3}$ and $\mu_1 = 105 \text{ cm}^2/\text{Vs}$ for the (hole) majority carriers and $n_2 = 1.24 \times 10^{17} \text{ cm}^{-3}$ and $\mu_2 = -3820 \text{ cm}^2/\text{Vs}$ for the (electron) minority carriers. In a second step, we calculate the transverse magnetoresistance for these parameters (red curve in Fig. S5B). It completely fails to describe the corresponding data. In fact, no negative magnetoresistance can arise in this setting. Thus, we conclude that two-band effects are not the cause of the observed nonlinearities in the low-temperature magnetotransport data.

D. Hall effect from odd-in-momentum Berry curvature: Conceptual basis and data

Here we provide supplementary information on the Hall effect contribution in $\text{Ce}_3\text{Bi}_4\text{Pd}_3$ that is due to this (noncentrosymmetric) material's odd-in- k Berry curvature $\Omega_z^{\text{odd}}(k)$ and leads to the observed spontaneous Hall effect as well as the even-in-magnetic field Hall component. The corresponding Hall conductivity σ_{xy} (see Eqn. 1 of the main part) depends on the out-of-equilibrium distribution function $f(k)$ under a driving electric field \mathcal{E}_x and will thus be field dependent, i.e., $\sigma_{xy} = \sigma_{xy}(\mathcal{E}_x)$. Thus, nonlinearities in terms of \mathcal{E}_x should appear.

In the perturbative treatment of Sodemann and Fu [32], σ_{xy} is linear in field,

$$\sigma_{xy}(\mathcal{E}_x) = \sigma_0 \cdot \mathcal{E}_x \quad , \quad (\text{S8})$$

where σ_0 is a constant, leading to a Hall current density

$$j_y = \sigma_{xy}(\mathcal{E}_x) \cdot \mathcal{E}_x = \sigma_0 \cdot \mathcal{E}_x^2 \quad (\text{S9})$$

that is quadratic in field. Under AC (1ω) excitation, this Hall current density appears as a 0ω and 2ω signal

$$j_y^{0\omega} = \sigma_0 \cdot \mathcal{E}_x^{1\omega} (\mathcal{E}_x^{1\omega})^* \quad \text{and} \quad j_y^{2\omega} = \sigma_0 \cdot (\mathcal{E}_x^{1\omega})^2 \quad . \quad (\text{S10})$$

In our experiments, we drive an electrical current I_x through the sample and measure a transverse voltage V_{xy} , and thus rewrite Eqn. S9 as

$$V_{xy} = \alpha I_x^2 . \quad (\text{S11})$$

This square-in-current Hall voltage should appear in both DC and AC experiments and we introduce the following nomenclature to distinguish the different effects:

$$V_{xy}^{\text{DC}} = \alpha^{\text{DC}} \cdot (I_x^{\text{DC}})^2 , \quad V_{xy}^{0\omega} = \alpha^{0\omega} \cdot (I_x^{1\omega})^2 , \quad V_{xy}^{2\omega} = \alpha^{2\omega} \cdot (I_x^{1\omega})^2 . \quad (\text{S12})$$

These expressions are related to the corresponding Hall current densities by $\mathcal{E}_x^{\text{DC},1\omega} = \rho_{xx} j_x^{\text{DC},1\omega} = \rho_{xx} I_x^{\text{DC},1\omega} / (wt)$ and $j_y^{\text{DC},0\omega,2\omega} = \sigma_{yy} \mathcal{E}_y^{\text{DC},0\omega,2\omega} = \sigma_{yy} V_y^{\text{DC},0\omega,2\omega} / l_y$. The latter equation represents a current density that is opposite in sign to the Hall current density of Eqn. S9, thus fulfilling the open-circuit condition $j_y = \sigma_{xy} \cdot \mathcal{E}_x + \sigma_{yy} \cdot \mathcal{E}_y = 0$, i.e., no net current flows in the y direction. Thus

$$\sigma_0 = \alpha \frac{1}{\rho_{xx}^3} \frac{w^2 t^2}{l_y} , \quad (\text{S13})$$

where we have used $\rho_{xx} = 1/\sigma_{xx} = 1/\sigma_{yy}$, which is exact for cubic symmetry, and where w , t , and l_y are the sample width, thickness, and transverse Hall contact distance, respectively. We will see that while we indeed observe these three contributions, other (linear-in-current, but still spontaneous or even-in-magnetic field) Hall voltage terms appear in addition. As discussed in Sect. IV C, we attribute them to the tilted Weyl-Kondo semimetal nature of $\text{Ce}_3\text{Bi}_4\text{Pd}_3$, which places the material in the fully nonequilibrium electric field regime already at the smallest fields we have applied.

First, we discuss the DC experiments. The longitudinal voltage V_{xx} is linear in I (defined as applied along x). This simple Ohmic behaviour demonstrates that the applied electric field has no appreciable effect on the material's bandstructure. By contrast, the spontaneous Hall voltage V_{xy} is nonlinear in I , and well described as the sum of a linear ($R_{xy}I$) and quadratic ($\alpha^{\text{DC}}I^2$) term (Fig. S6A). Both emerge only as Kondo coherence sets in at low temperatures (Fig. S6B and Fig. 2F of the main part). Only the quadratic-in-field (or current) response was predicted in ref [32]. The joint appearance of the linear-in-field term strongly suggests that both phenomena have a common origin (see Sect. IV C for its discussion). That the emergence of a spontaneous Hall voltage is due to a thermodynamically as opposed to microscopically broken TRS (as in magnetic systems) is further discussed in Sect. I E.

Next, we address nonlinearities in our AC experiments. We observe both a 2ω and a 0ω spontaneous Hall voltage in response to a 1ω current excitation (Fig. 2D, E of the main part and Fig. S7A).

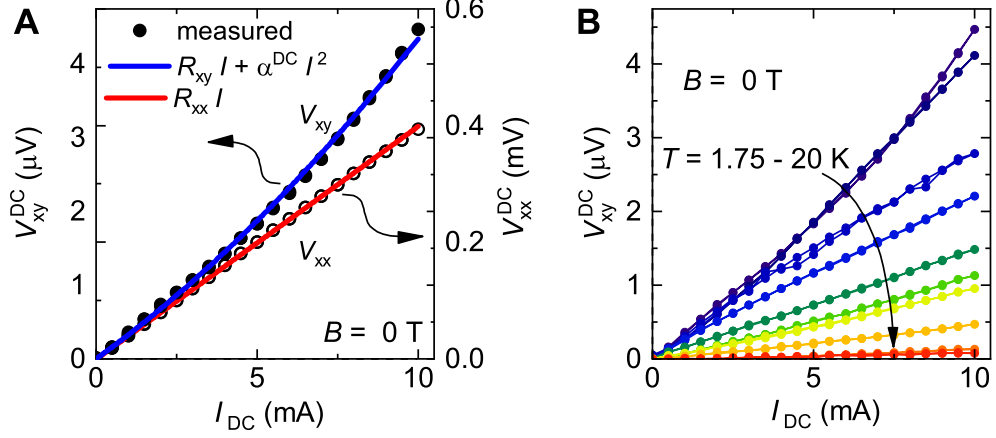


FIG. S6: **Nonlinearity of the spontaneous Hall effect in DC transport.** (A) Current-voltage characteristics in zero magnetic field for the transverse (full symbols, left axis) and longitudinal (open symbols, right axis) voltage of $Ce_3Bi_4Pd_3$ at 1.75 K. The nonlinearity in the Hall response is quantified by α^{DC} . (B) Temperature evolution of the current-voltage characteristic of the Hall component in zero magnetic field.

Both emerge only upon entering the Kondo coherent regime (Fig. 2F of the main part). In addition

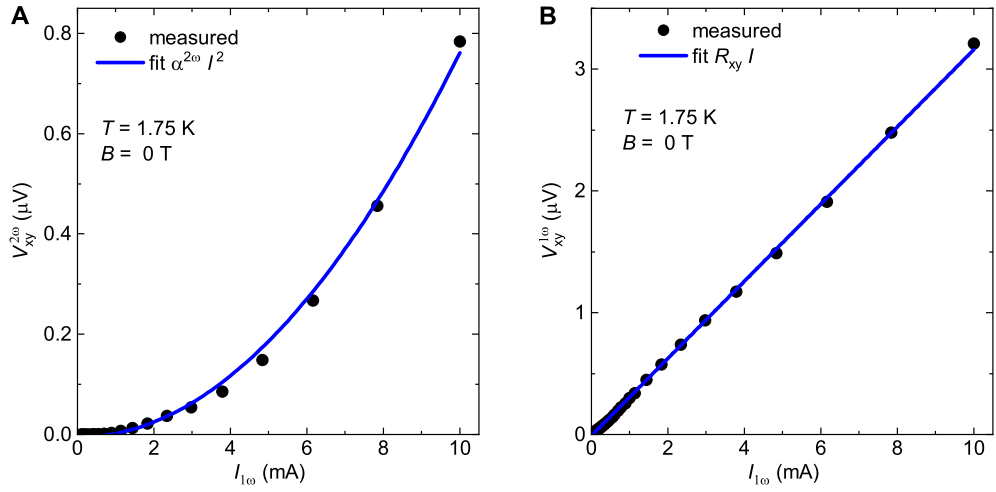


FIG. S7: **Nonlinearity of the spontaneous Hall effect in AC transport.** (A) Second harmonic Hall voltage of $Ce_3Bi_4Pd_3$ in response to an AC excitation in zero magnetic field and at 1.75 K. The blue curve is a quadratic fit to the data, with the fitting parameter $\alpha^{2\omega}$. (B) First harmonic, linear-in-current Hall voltage measured under the same condition as in panel (A). The blue line is a linear fit to the data, with the slope R_{xy} . The measurement was done on the same sample as in

Fig. S6.

to these two contributions, which were predicted in ref[32], we also find a robust 1ω spontaneous Hall signal, that closely follows the linear-in-current signal of our DC experiment (Fig. 2B of the main part and Fig. S7B). Both display a pronounced linear σ_{xy} vs. σ_{xx} relationship in the Kondo coherent regime (grey shaded area in Fig. 2B of the main part, temperature is an implicit parameter). In terms of absolute values, this is the dominant signal; it is of the order of the 3D conductivity quantum $e^2/(ha)$, where a is the lattice parameter. The absolute values of the different contributions are given in Table S1.

TABLE S1: Absolute values of the spontaneous Hall response of single crystal S2, with current approximately along $[111]$, as defined in Fig. 2 of the main part.

	2ω	0ω	$\text{DC-}I^2$	1ω	$\text{DC-}I$
T_{H} (K)	3.8	4.6	4.3	4.8	4.9
α^{max} ($10^{-3} \mu\text{V}/\text{mA}^2$)	7.67	10.8	14.3		
ρ_{xy}^{max} ($\mu\Omega\text{m}$)				0.21	0.18

We stress that the spontaneous Hall response is robust in all channels (linear-in- I and quadratic-in- I Hall voltage in DC experiments, and 0ω , 1ω , and 2ω Hall voltage in AC experiments). Among the many samples we have measured, not a single one did not show a spontaneous Hall effect. For the three samples we have studied in depth (three single crystals from different growth batches, with current excitation approximately along $[103]$, $[100]$, and $[111]$, respectively), all features are very similar (Fig. S8). In terms of absolute values, $\tan \Theta_{\text{H}}$ (in the linear-in- I response for crystal S1 and in the 1ω response for crystals S2 and S3) is 0.19, 0.52, and 0.17, respectively.

Finally, we comment on effects in a finite applied magnetic field B . Here, Hall contributions associated with the odd-in- k Berry curvature are detected as even-in- B contributions, which is how we separate them from other (normal, anomalous, two-band ...) contributions, which are all odd in B . Again, such even-in- B contributions appear in all channels (see Fig. 2D, E and Fig. 3C, D) and represent the same physics discussed in the main part. The only role the magnetic field plays here is to successively suppress the odd-in- B Hall contribution, similar to what happens when enhancing the temperature above the Kondo coherence temperature.

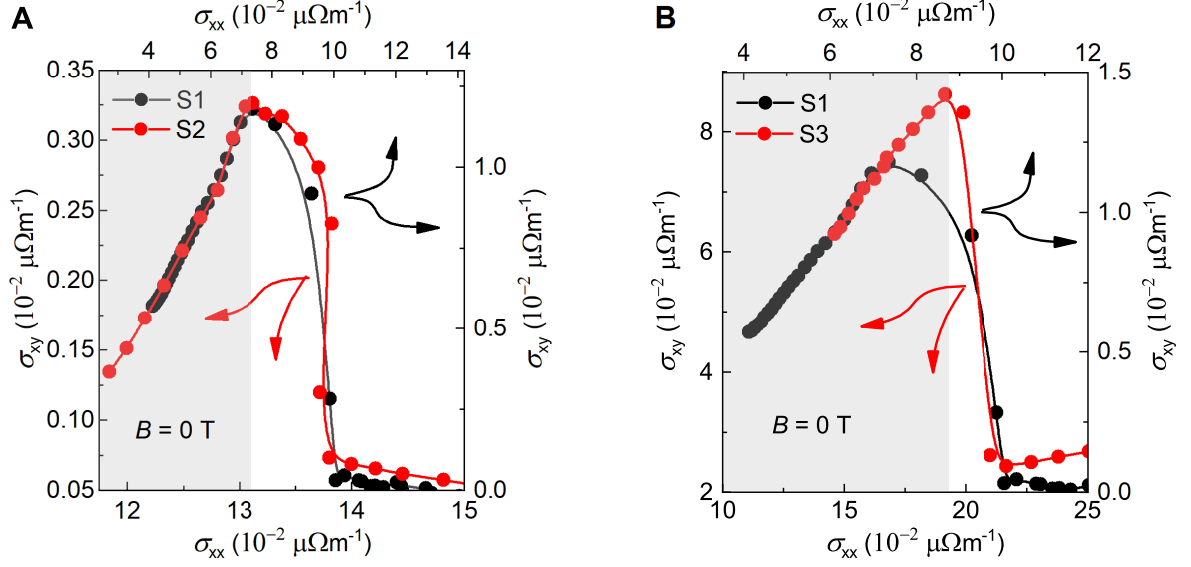


FIG. S8: **Reproducibility of the spontaneous Hall effect.** Linear-in-current spontaneous Hall signal, shown as σ_{xy} vs. σ_{xx} , where temperature is an implicit parameter, for samples from three different growth batches and orientations (current approximately along [103], [111], and [100] for crystals S1, S2, and S3, respectively). S1 was measured with DC current in quasi-AC mode, S2 and S3 are 1ω signals from AC experiments. (A) Comparison of crystals S1 and S2. (B) Comparison of crystals S1 and S3. The grey shading indicates the Kondo coherent regime, where

$$\sigma_{xy} \text{ is linear in } \sigma_{xx}.$$

E. Berry curvature-driven Hall effect and macroscopic TRS breaking

The Berry curvature-driven Hall effect of a noncentrosymmetric material with (microscopically) preserved TRS (Eqn. 1), though measured under zero magnetic field, is a nonlinear response effect to an applied electric field \mathcal{E}_x . As such it is inherently dissipative, causing TRS breaking on the thermodynamic level. This is in contrast to the linear response regime in which the normal (Lorentz force-driven) Hall effect can be considered.

The nonlinear response is determined by the distribution function in the presence of the external drive, which breaks TRS even if the system in equilibrium obeys TRS. In fact, the corresponding Hall conductivity σ_{xy} is defined only in the presence of an electric field, and hence in a state that produces entropy (at the rate $\dot{S} = j_x \mathcal{E}_x$) and breaks TRS thermodynamically. In other words, in the limit of zero entropy production, that is for $\mathcal{E}_x \rightarrow 0$, also $\sigma_{xy} \rightarrow 0$.

This is in contrast to electrical transport in the framework of linear response theory, where the

transport coefficients are expressed in terms of correlation functions in the absence of a driving field. As a consequence these correlation functions reflect the TRS of the system in equilibrium. Thus, even though an applied electric field by itself breaks TRS on the thermodynamic level, the linear response transport coefficients are still well defined when the entropy production is vanishing, i.e., for $\mathcal{E}_x \rightarrow 0$ the Hall conductivity remains finite.

F. Odd-in-current contribution to Berry-curvature driven Hall voltage

The Berry curvature-driven Hall current density in an IS breaking but TRS preserving material is given by

$$j_y = \frac{e^2}{\hbar} \int \frac{d^3k}{(2\pi)^3} f(\mathbf{k}) \underbrace{\Omega_z^{\text{odd}}(\mathbf{k}) \mathcal{E}_x}_{v_y} \quad (\text{S14})$$

where $f(\mathbf{k})$ is the out-of-equilibrium distribution function associated with an applied electric field \mathcal{E}_x and v_y is the anomalous velocity. The specific dependence of the Hall voltage on the current, $V_{xy}(I_x)$, associated with Eqn. S14 depends on the form of $f(\mathbf{k})$. In a linearized Boltzmann approximation (as used in refs [32, 35]), $f(\mathbf{k})$ corresponds to the equilibrium (Fermi-Dirac) distribution function $f_0(\mathbf{k})$ rigidly shifted in the direction of \mathcal{E}_x , that is $f(\mathbf{k}) = f_0(\mathbf{k}) + \partial f_0 / \partial k_x \cdot \delta k_x$, with $\delta k_x = (e\tau/\hbar) \cdot \mathcal{E}_x$. In this case, Eqn. S14 simplifies to [32]

$$j_y^{(2)} = \frac{e^3 \tau \mathcal{E}_x^2}{\hbar^2} \underbrace{\int \frac{d^3k}{(2\pi)^3} \frac{\partial f_0(\mathbf{k})}{\partial k_x} \Omega_z^{\text{odd}}(\mathbf{k})}_{D_{zx}}, \quad (\text{S15})$$

where D_{zx} is the Berry curvature dipole and the superscript (2) makes it explicit that this is a 2nd order effect in \mathcal{E}_x , i.e., j_y is quadratic and thus even in \mathcal{E}_x . However, this picture fails to consider the boundary condition of a Hall effect experiment, namely that no net current can flow in the y -direction (see Sect. I D, text below Eqn. S12). To fulfill this condition, the above current $j_y^{(2)}$ must be compensated by an equal current of opposite sign, that can only be generated by a shift of the Fermi surface in the k_y direction by $\delta k_y = (e\tau/\hbar) \cdot \mathcal{E}_y^{(2)}$, with $\mathcal{E}_y^{(2)} = -\rho_{xx} j_y^{(2)}$. In a second step, this shift then leads to an additional Berry curvature-driven Hall current density $j_y^{(3)}$, by populating states with finite anomalous velocity $v_y(\mathbf{k})$.

To be explicit, the (extra) shift of $f(\mathbf{k})$ by δk_y ,

$$f(\mathbf{k} + \delta \mathbf{k}_y) = f_0(\mathbf{k}) + \delta k_x \frac{\partial f_0(\mathbf{k})}{\partial k_x} + \delta k_y \frac{\partial f_0(\mathbf{k})}{\partial k_y}, \quad (\text{S16})$$

results in an extra contribution (3rd term) which, through Eqn.S14 and with $\delta k_y = -(e^4 \tau^2 \rho_{xx} / \hbar^3) \cdot D_{zx} \mathcal{E}_x^2$, drives the (3rd order) Hall current density

$$j_y^{(3)} = -\left(\frac{e^3 \tau}{\hbar^2}\right)^2 \rho_{xx} D_{zx} D_{zy} \mathcal{E}_x^3, \quad (\text{S17})$$

where $D_{zy} = \int d^3k / (2\pi)^3 (\partial f_0(\mathbf{k}) / \partial k_y) \Omega_z^{\text{odd}}(\mathbf{k})$ is the corresponding Berry curvature dipole. Combining Eqns. S15 and S17, the Hall voltage V_{xy} will be the sum of both even-in- I_x and odd-in- I_x contributions.

G. Trivial Hall contribution from crystal symmetry

Finally, we note that in systems with low enough crystalline symmetry (lower than cubic), the resistivity tensor cannot be represented by a simple scalar. As a consequence, a Hall-like linear-in- \mathcal{E} (1ω) signal might appear if the electric field \mathcal{E} is applied off-axis with respect to the main crystallographic directions.

However, $\text{Ce}_3\text{Bi}_4\text{Pd}_3$ is cubic and thus no such (trivial) perpendicular component can arise. This can be readily understood: For a cubic system, the three eigenvalues of the conductivity matrix are equal to each other; in other words, the conductivity matrix is a constant multiplied by a unit matrix. In this case, regardless of the direction along which the drive electric field is applied, the induced current from this mechanism will always be along the direction of the applied field, and there is no Hall response. Note that the Weyl-Kondo phase in equilibrium preserves the crystalline symmetry.

One can make this rather transparent point more formally by perturbatively solving the Boltzmann equation for the non-equilibrium distribution function f and see that this “trivial” mechanism would in general yield 1ω , 3ω *etc.* contributions to the Hall response. However, for the cubic system, the contributions vanish. We can illustrate the point by considering the leading order (responsible for any 1ω response)

$$f_1^\omega = \frac{e\tau \mathcal{E}_a \partial_a f_0}{1 + i\omega\tau},$$

where f_0 is the equilibrium distribution, and the repeated indices mean summation over. In turn, the 1ω anisotropic electric currents induced by the “normal” velocity term is

$$j_a^\omega = -e \int_k \partial_a \epsilon_k f_1^\omega. \quad (\text{S18})$$

Combining these equations, we find the normal-velocity induced 1ω current to be

$$j_a^\omega = -\frac{e^2\tau}{1+i\omega\tau} \int_k (\partial_a \epsilon_k) (\partial_\mu f_0) \mathcal{E}_\mu . \quad (\text{S19})$$

An electric field \mathcal{E} applied in an arbitrary direction can be expressed as the combination of its components along the three principle axes, *i.e.*, $\mathcal{E} = \mathcal{E}_x \hat{x} + \mathcal{E}_y \hat{y} + \mathcal{E}_z \hat{z}$. According to Eqn. (S19), \mathcal{E}_x only induces a current along \hat{x} (otherwise, the integral is over an odd function and vanishes): $j_x^\omega = \sigma_{xx} \mathcal{E}_x$. Likewise, \mathcal{E}_y induces a current along \hat{y} ; and \mathcal{E}_z induces a current along \hat{z} . Moreover, $\sigma_{xx} = \sigma_{yy} = \sigma_{zz}$. Thus, the induced current must be along the electric field, regardless of the direction the electric field is applied, and there is no Hall response.

H. Imprint of Berry curvature-driven Hall effect on electrical resistivity

We observe that the onset of spontaneous Hall effect with decreasing temperature leaves an imprint also on the (longitudinal) electrical resistivity (Fig. S2). This effect is understood as follows: Firstly, there is a trivial source, a transverse direction misalignment of the electrical resistance contacts (Fig. S1), that is explained in detail in Sect. I A. Secondly, there is an intrinsic source, which is discussed in what follows.

The appearance of a Hall voltage is associated with a reconstruction of the current path in the sample, charge carriers being accumulated on one side of the sample (hence the Hall voltage). This will not affect the longitudinal resistivity appreciably if the tangent of the Hall angle, $\tan \Theta_H = \mathcal{E}_y / \mathcal{E}_x = \sigma_{xy} / \sigma_{xx}$, is small. However, with the giant values we observe ($\tan \Theta_H$ up to 0.5, see main text), we are not in this limit and hence do observe a nonnegligible effect. To be explicit, the resistivity ρ_{xx} depends on $\tan \Theta_H$ as

$$\rho_{xx} = \frac{\sigma_{xx}}{\sigma_{xx}^2 + \sigma_{xy}^2} = \frac{1}{\sigma_{xx}} \frac{1}{1 + \tan^2 \Theta_H} \quad (\text{S20})$$

Thus, as $\tan \Theta_H$ increases upon the onset of the spontaneous Hall effect, ρ_{xx} should drop. To test this scenario, we plot the relative change of resistivity across the onset of the spontaneous Hall effect as a function of temperature (Fig. S9A-C). Indeed, we observe the expected drop for all three samples studied. Moreover, we observe that the relative drop size increases with $\tan \Theta_H$, and that the magnitude and functional form of the dependence (Eqn. S20) is in overall agreement with the data. This provides strong evidence that the drop in R_{xx} is indeed due to this intrinsic effect.

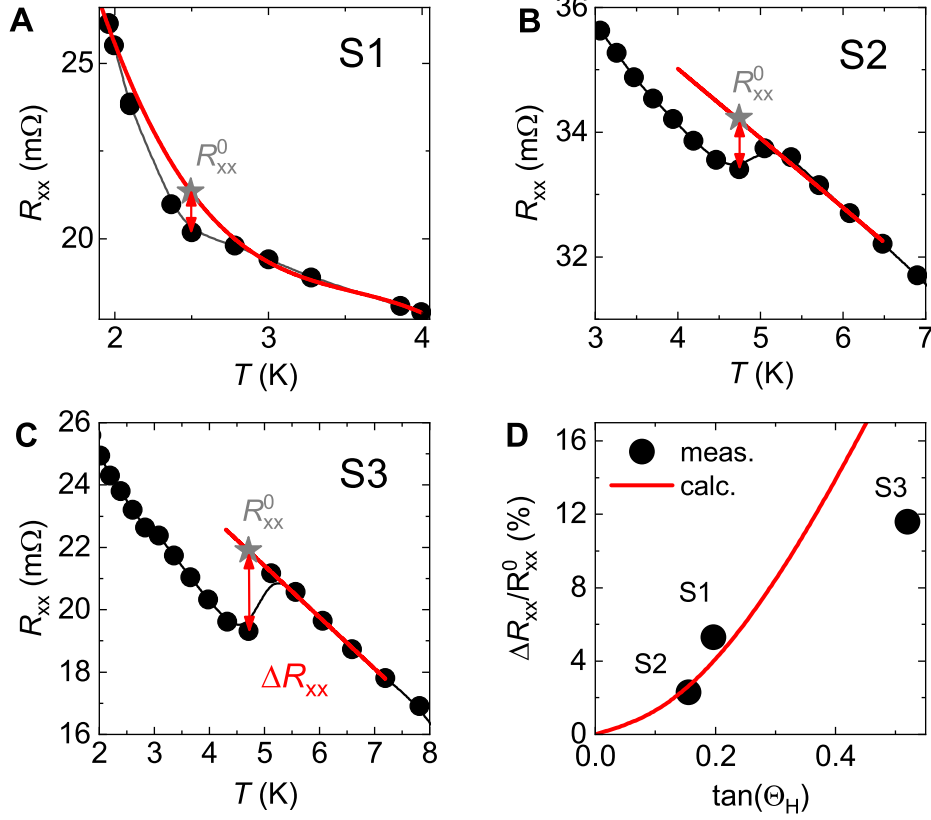


FIG. S9: **Resistance change due to large Hall angle.** (A-C) Longitudinal electrical resistance R_{xx} , corrected for contact misalignment (Fig. S1), for samples S1, S2, and S3. With decreasing temperature, a drop of R_{xx} is observed at the onset of the spontaneous Hall effect. For a rough estimate of its magnitude, $R_{xx}(T)$ above the onset temperature is extrapolated to lower T and the difference ΔR_{xx} is read off the data as indicated (red double arrow). (D) Relative resistance change $\Delta R_{xx}/R_{xx}^0$ of the three sample (symbols) vs. the tangent of the Hall angle (determined at low temperatures where the spontaneous Hall effect is fully established), defined as $\tan \Theta_H = \partial\sigma_{xy}/\partial\sigma_{xx}$ (see Fig. S8). Clearly, $\Delta R_{xx}/R_{xx}^0$ increases with $\tan \Theta_H$. The red line shows the expectation from Eqn. S20, $\Delta\rho_{xx}/\rho_{xx}^0 = (\rho_{xx}^0 - \rho_{xx})/\rho_{xx}^0 = 1 - 1/(1 + \tan^2 \Theta_H)$, with no adjustable parameter. The overall agreement, both in terms of magnitude and shape, further underpins that the observed signatures in R_{xx} are intrinsic and due to the giant magnitude of the Hall angle.

That the Hall angle is different for the different samples is, most likely, due to the different current directions with respect to the crystal axes. Preliminary results on a single crystal contacted several times to achieve different current directions reveal a sinusoidal variation of the magnitude

of the spontaneous Hall resistivity with angle. Such a dependence is expected for a Berry-curvature driven Hall effect.

II. μ SR, MAGNETIZATION, AND SPECIFIC HEAT

A. Analysis of μ SR data

Due to the large muon gyromagnetic ratio and the availability of 100% spin-polarized muon beams, ZF- μ SR is one of the most sensitive probes for detecting small spontaneous magnetic fields. Consequently, the technique has been successfully used to determine the occurrence (or the absence) of TRS breaking in many different materials [46–48]. If TRS is broken, the onset of tiny spontaneous currents gives rise to associated (weak) magnetic fields, detected by ZF- μ SR as an increase in the muon spin relaxation rate.

In nonmagnetic materials in zero field, the relaxation is typically dominated by the randomly oriented nuclear moments (in our case by the $4.11\mu_N$ nuclear moments of ^{209}Bi), which can be described by the Gaussian Kubo-Toyabe relaxation function [49]

$$G_{\text{KT}} = \frac{1}{3} + \frac{2}{3}(1 - \sigma^2 t^2) e^{-\frac{\sigma^2 t^2}{2}} . \quad (\text{S21})$$

A possible electronic contribution to the ZF- μ SR spectra is modeled by an additional Lorentzian relaxation, with the electronic relaxation rate denoted by Λ . The total relaxation is then described by

$$A_{\text{ZF}} = A_s G_{\text{KT}} e^{-\Lambda t} + A_{\text{bg}} , \quad (\text{S22})$$

where A_s and A_{bg} are the sample- and background-related asymmetries, respectively, the latter being about 15% of the former in our case.

The ZF- μ SR data of $\text{Ce}_3\text{Bi}_4\text{Pd}_3$ taken at 10 and 0.26 K essentially collapse on top of each other (Fig. S10), providing direct evidence that no magnetization develops in this temperature range. Fits to all data sets were performed using the `musrfit` suite [50], with the raw error bars reflecting the data counting statistics and the fit parameter uncertainties resulting from standard error propagation methods. The resulting fit parameters reveal that the depolarization is mostly of nuclear origin, which is further confirmed by the prompt recovery of the signal in a very small longitudinal magnetic field (Fig. S10). The electronic relaxation rate is very small and temperature

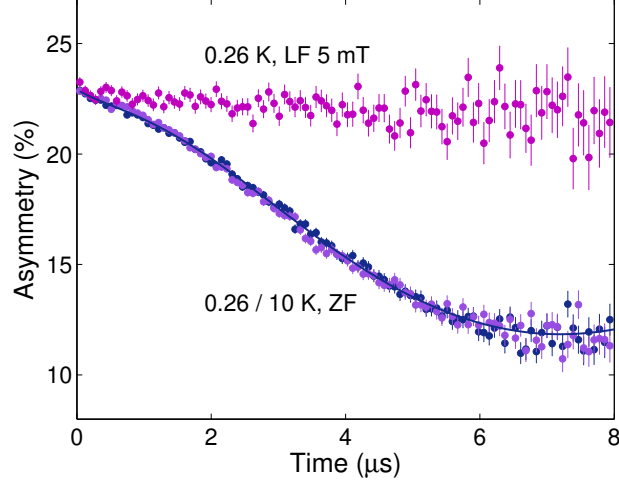


FIG. S10: **ZF- μ SR detects no TRS breaking in $\text{Ce}_3\text{Bi}_4\text{Pd}_3$.** ZF- μ SR spectra at 0.26 and 10 K, and 5 mT longitudinal-field (LF) spectrum at 0.26 K. The complete overlap of the two ZF spectra is direct evidence that no magnetization develops in this temperature range. The weak muon spin depolarization is mostly of nuclear origin, as confirmed by its prompt recovery in a very small field. The solid line is a fit to the spectra by means of Eqn. S22.

independent within the error bars (see Fig. 2C of the main part). This is unambiguous evidence that, in the studied temperature range, TRS is preserved in $\text{Ce}_3\text{Bi}_4\text{Pd}_3$.

B. Magnetization

As discussed above, ZF- μ SR is the most sensitive probe to detect TRS breaking, which may for instance be caused by a magnetic phase transition (even if partial or due to a minority foreign phase), and has clearly ruled it out. Nevertheless, to corroborate this finding with a more common tool, we have performed field-swept measurements of the magnetization at temperatures below the onset of the spontaneous Hall effect (Fig. S11). Any even spurious ferromagnetic transition would lead to hysteretic behavior. Clearly, no hysteresis is observed, neither in sweeps up to high fields (up to 2.5 T, panel A), nor in precise very low-field sweeps (up to 0.15 T, panel B). In fact, the $M(B)$ curves in both field ranges show a smooth, linear behavior, as expected for a paramagnetic phase.

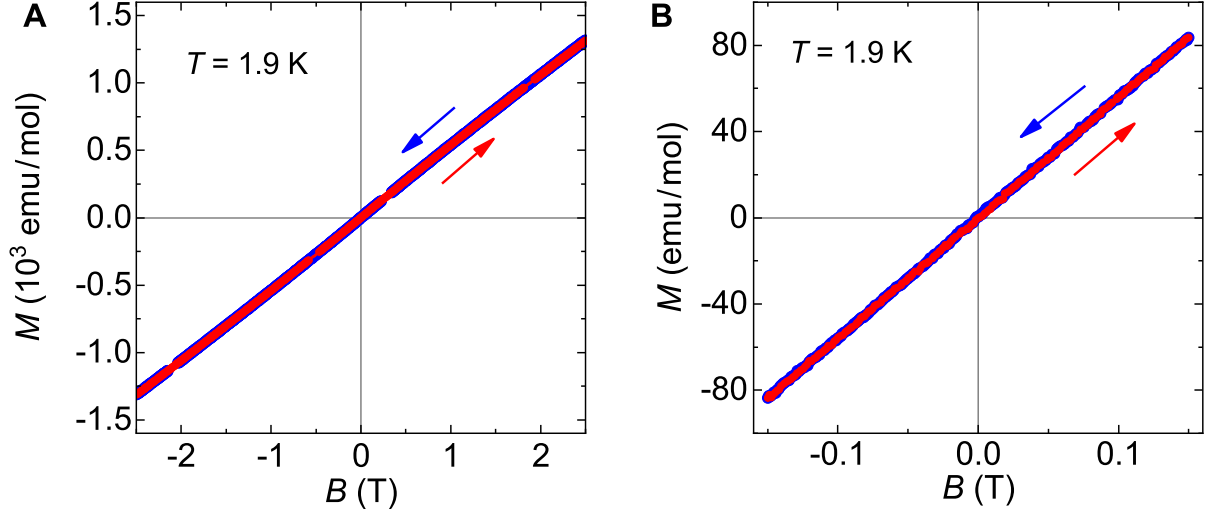


FIG. S11: **Absence of hysteresis in the magnetization.** Magnetization loops of $\text{Ce}_3\text{Bi}_4\text{Pd}_3$ in fields up to 2.5 T (left) and higher accuracy measurement in fields up to 150 mT (right), both revealing the absence of any hysteretic behavior. The symbol sizes for up (red) and down (blue) sweeps are different for better visibility. The initial magnetization curve is contained in the up sweep.

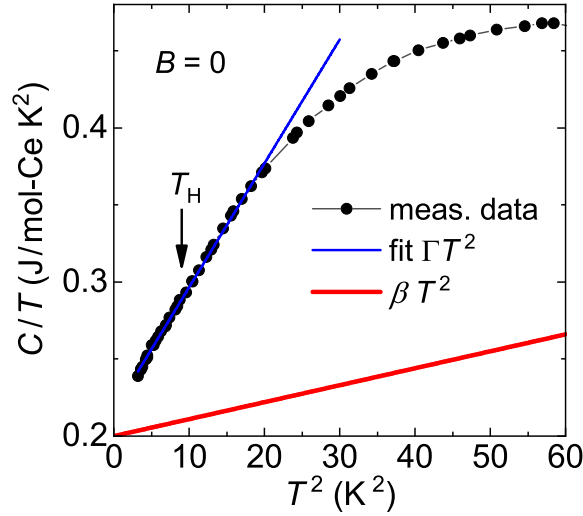


FIG. S12: **Specific heat of $\text{Ce}_3\text{Bi}_4\text{Pd}_3$.** Specific heat data in zero magnetic field, plotted as C/T vs. T^2 (black dots), for the batch of sample S1. The data follow a linear behavior (blue line) with a slope that overshoots the Debye phonon term (red line, offset for clarity, taken from ref [24]), as expected for a Weyl-Kondo semimetal. No phase transition is discerned, neither at the onset of the spontaneous Hall effect (T_H), nor elsewhere.

C. Specific heat

Specific heat measurements are the most direct tool to detect phase transitions, be it with or without TRS breaking. In Fig. S12 we show the specific data for the batch of sample S1, taken at zero magnetic field and plotted as C/T vs. T^2 . As seen previously [24], an enhanced $C/T = \Gamma T^2$ term [with $\Gamma = 0.008 \text{ J}/(\text{mol-Ce K}^4)$, corresponding to a low quasiparticle velocity of about 1000 m/s] is observed, evidencing very flat linearly-dispersing electronic bands, one of the hallmarks of a Weyl-Kondo semimetal [24, 25].

No phase transition anomaly is seen in the data. Most notably, at the onset temperature of the spontaneous Hall effect (T_H), the data vary smoothly, following the C/T vs. T^2 law without any detectable deviation.

In summary, our ZF- μ SR, magnetization, and specific heat data rule out that the observed spontaneous and even-in-magnetic field Hall effect seen in our $\text{Ce}_3\text{Bi}_4\text{Pd}_3$ samples is due to extrinsic effects.

III. DENSITY FUNCTIONAL THEORY CALCULATIONS

For the density functional theory (DFT) bandstructure calculations of $\text{Ce}_3\text{Bi}_4\text{Pd}_4$ we used the all-electron augmented-plane-wave code WIEN2k [51] with the Perdew, Burke, Ernzerhof (PBE) functional [52]. The experimentally determined structure [53] was used with space group $I\bar{4}3d$, $a = 10.052 \text{ \AA}$, and Ce, Pd, and Bi at the $12a$, $12b$, and $16c$ (with $x = 0.0839$) positions, respectively. As DFT cannot treat many body effects such as the Kondo interaction of the Ce $4f$ electrons with the conduction electrons derived from s , p , and d orbitals, we use it here to describe the conduction electron part only. For this purpose, we use the open-core approximation, where one Ce $4f$ electron is included as noninteracting core state, but the $4f$ basis functions are removed from the bandstructure calculations and thus cannot hybridize with other orbitals. As such, this approach is the *ab initio* counterpart of H_c in the periodic Anderson Hamiltonian of the Weyl-Kondo model (Eqn. S23).

We used atomic sphere radii of 3.0, 2.5, and 2.5 Bohr for Ce, Pd and Bi, respectively, and a plane wave cutoff parameter of $RK_{\text{max}} = 8.5$, where $R = 2.5$ and K_{max} restricts the plane wave expansion. Inside the atomic spheres an angular momentum expansion up to $l_{\text{max}} = 10$ is used, while for the nonspherical matrix elements l_{max} is restricted to 6. The \mathbf{k} -space integration was

TABLE S2: Coordinates of Weyl nodes in the k_x - k_z plane of the Brillouin zone of $\text{Ce}_3\text{Bi}_4\text{Pd}_3$, in units of $2\pi/a$, where $a = 10.052 \text{ \AA}$, and their energies with respect to the Fermi energy in eV.

Due to the cubic symmetry of the system, all coordinates occur in both signs and all x, y, z permutations, leading to a multiplicity of 24.

Weyl node	k_x	k_y	k_z	E
1	0.517	0	0.174	-0.127
2	0.447	0	0.164	-0.174
3	0.372	0	0.112	-0.196
4	0.172	0	0.087	-0.282

done with an $18 \times 18 \times 18$ \mathbf{k} mesh. Spin-orbit coupling was included in a second variational procedure [51].

To identify the Weyl nodes, we used a modified version of BerryPI [54] that calculates the Berry curvature of Wilson loops around candidate Weyl nodes [55]. Within the k_x - k_z plane of the Brillouin zone, we have identified 4 Weyl nodes (see Fig. 4A of the main part) with the coordinates and energies given in Table S2. All Weyl nodes are situated at least 100 meV away from the Fermi level. We expect that the Kondo interaction will pin (part of) these Weyl nodes to the Fermi level, just as it does in the Weyl-Kondo model (Sect. IV A). The Weyl node 1 with sizeable tilt might be a good candidate for this process. Whereas in previous DFT + dynamical mean field theory (DMFT) calculations for $\text{Ce}_3\text{Bi}_4\text{Pd}_3$ [56] topologically nontrivial band crossings were not considered, a very recent study [57] suggests that nodal lines are also present in the uncorrelated (DFT) bandstructure, far above the Fermi level. The low-temperature specific heat of $\text{Ce}_3\text{Bi}_4\text{Pd}_3$ [24], however, is consistent with a scenario where Weyl point (as opposed to line) nodes are driven by the Kondo effect to the immediate vicinity of the Fermi energy (as described by our Weyl-Kondo model, Sect. IV A).

IV. THEORETICAL TREATMENT OF TILTED WEYL-KONDO SEMIMETAL MODEL

A. Microscopic model

To study the effect of the Kondo interaction on a conduction electron band with tilted Weyl cones, we generalize a previously established Weyl-Kondo semimetal model [25] (for which the role of nonsymmorphic space-group symmetry was recently emphasized [58]) to the case with tilting. The periodic Anderson model reads

$$H = H_c + H_{cd} + H_d \quad , \quad \text{with} \quad (\text{S23})$$

$$H_c = \sum_{\mathbf{k}} \Psi_{\mathbf{k}}^\dagger h_{\mathbf{k}} \Psi_{\mathbf{k}} \quad , \quad \text{where} \quad (\text{S24})$$

$$\Psi_{\mathbf{k}}^T = \left(c_{\mathbf{k}\uparrow,A} \quad c_{\mathbf{k}\uparrow,B} \quad c_{\mathbf{k}\downarrow,A} \quad c_{\mathbf{k}\downarrow,B} \right) \quad , \quad \text{and}$$

$$h_{\mathbf{k}} = \sigma_0 [u_1(\mathbf{k})\tau_x + u_2(\mathbf{k})\tau_y + m\tau_z] + \lambda[\mathbf{D}(\mathbf{k}) \cdot \boldsymbol{\sigma}]\tau_z + C[m - \lambda D(\mathbf{k})]\sigma_0\tau_0 \quad ,$$

$$H_{cd} = V \sum_{i,\sigma} \left(d_{i\sigma}^\dagger c_{i\sigma} + \text{H.c.} \right) \quad , \quad \text{and} \quad (\text{S25})$$

$$H_d = E_d \sum_{i,\sigma} d_{i\sigma}^\dagger d_{i\sigma} + U \sum_i n_{i\uparrow}^d n_{i\downarrow}^d \quad . \quad (\text{S26})$$

Here, H_c , H_{cd} , and H_d are the conduction electron term, hybridization term, and strongly correlated d electron term (representing the physical $4f$ electrons), respectively. The notations are the same as in ref [25]. In particular, $u_1(\mathbf{k})$ and $u_2(\mathbf{k})$ are determined by the conduction electron hopping, $t_{\langle ij \rangle} = t$ between nearest-neighbor sites ($\langle\langle ij \rangle\rangle$). The second term specifies a Dresselhaus-type spin-orbit coupling between the second-nearest-neighbor sites ($\langle\langle\langle ij \rangle\rangle\rangle$), which is of strength λ and involves vector $\mathbf{D}(\mathbf{k}) = (D_x(\mathbf{k}), D_y(\mathbf{k}), D_z(\mathbf{k}))$. Specifically,

$$u_1(\mathbf{k}) = t \left(1 + \sum_{n=1}^3 \cos(\mathbf{k} \cdot \mathbf{a}_n) \right) \quad , \quad (\text{S27})$$

$$u_2(\mathbf{k}) = t \sum_{n=1}^3 \sin(\mathbf{k} \cdot \mathbf{a}_n) \quad , \quad (\text{S28})$$

$$D_x(\mathbf{k}) = \sin(\mathbf{k} \cdot \mathbf{a}_2) - \sin(\mathbf{k} \cdot \mathbf{a}_3) - \sin(\mathbf{k} \cdot (\mathbf{a}_2 - \mathbf{a}_1)) + \sin(\mathbf{k} \cdot (\mathbf{a}_3 - \mathbf{a}_1)) \quad , \quad (\text{S29})$$

and D_y , D_z are obtained by permuting the fcc primitive lattice vectors $\mathbf{a}_{n=1,2,3}$. Additionally, $\boldsymbol{\sigma} = (\sigma_x, \sigma_y, \sigma_z)$ and $\boldsymbol{\tau} = (\tau_x, \tau_y, \tau_z)$ are the Pauli matrices acting on the spin and sublattice spaces, respectively, and σ_0 is the identity matrix. The last term in H_c , $C[m - \lambda D(\mathbf{k})]\sigma_0\tau_0$, is the tilt (or ‘‘C’’) term and has not been considered before. Here, $D(\mathbf{k}) \equiv |\mathbf{D}(\mathbf{k})| =$

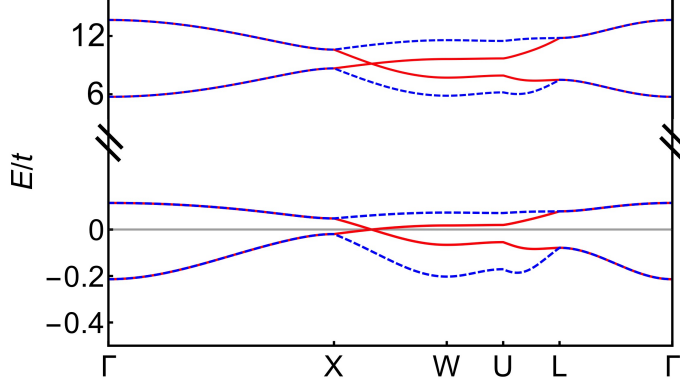


FIG. S13: **Kondo interaction pins tilted Weyl nodes to Fermi energy.** Dispersion for the tilted Weyl-Kondo semimetal model of Eqns. S23-S26, with energy in units of the hopping amplitude t , the Fermi energy at $E/t = 0$, and the parameters $(t, \lambda, m, E_d, V, C) = (1, 0.5, 1, -6, 6.6, 0.9)$; in the resulting saddle-point solution, $r \simeq 0.2614$ and $\ell \simeq 6.3366$. The nonzero C term causes the Weyl nodes to be tilted, which is seen in the dispersion near the Weyl nodes between X and W. The upper quartet of bands, with the bandwidth D/t of the conduction electrons, is a remnant of the solution in the absence of the Kondo effect. That it contains Weyl nodes far away from the Fermi level captures the conduction-electron only solution of our open-core DFT calculations (Fig. 4A). The lower quartet of bands, with strongly renormalized bandwidth ($k_B T_K/t$, where T_K is the Kondo temperature), appears only in the presence of the Kondo interaction. It contains emergent Weyl nodes at the Fermi energy. Away from the commensurate filling used here, they will be situated slightly away from the Fermi level, as sketched in Fig. 4B.

$\sqrt{D_x(\mathbf{k})^2 + D_y(\mathbf{k})^2 + D_z(\mathbf{k})^2}$. Physically, the C term represents kinetic hopping that goes beyond the nearest-neighboring sites.

By solving the self-consistent saddle-point equations for the strong interaction limit ($U = \infty$), we find a Weyl-Kondo solution in the presence of the C term. Specifically, we follow the approach in ref [25] to take care of the prohibition of d fermion double occupancy by an auxiliary-particle method [59], which rewrites $d_{i\sigma}^\dagger = f_{i\sigma}^\dagger b_i$. The $f_{i\sigma}^\dagger$ (b_i) are fermionic (bosonic) operators, which satisfy a constraint that is enforced by a Lagrange multiplier ℓ . This approach leads to a set of saddle-point equations, where b_i condenses to a value r . The d fermion level and the hybridization get renormalized as $E_d \rightarrow E_d + \ell$ and $V \rightarrow rV$. Figure S13 describes the renormalized bands, and illustrates the tilting of the Weyl-Kondo cone at the Fermi energy.

B. Berry curvature induced Hall response of titled Weyl-Kondo semimetal: Perturbative regime

To illustrate the role of the tilting term in the Weyl-Kondo semimetal, we first consider the weak-field limit. Here, it was shown [32] that the Hall conductivity σ_{xy} contains only 2ω (and the associated 0ω) components and is determined by the Berry curvature dipole \mathbf{D} , a rank-2 tensor with components $D_{ab=x,y,z}$ that are expressed as

$$D_{ab} = \int \bar{d}^3k f_0(\varepsilon_{\mathbf{k}}) \partial_{ka} \Omega_b(\mathbf{k}) \quad (\text{S30})$$

$$= \oint_{\text{FS}} \bar{d}^2k \frac{v_a(\mathbf{k}) \Omega_b(\mathbf{k})}{v(\mathbf{k})} \quad , \quad (\text{S31})$$

where $\bar{d}^n k \equiv d^n k / (2\pi)^n$, $\partial_{ka} \equiv \partial / \partial k_a$, $v_a(\mathbf{k}_F) = \partial_{ka} \varepsilon_{ka}$ is the velocity, and $f_0(\varepsilon_{\mathbf{k}})$ is the equilibrium (Fermi-Dirac) distribution function of eigenenergy $\varepsilon_{\mathbf{k}}$, with the Fermi energy being set to 0; at $T \rightarrow 0$, $f_0(\varepsilon_{\mathbf{k}}) = \Theta(-\varepsilon_{\mathbf{k}})$. We consider the Fermi pockets to surround the Weyl nodes, and have used the Jacobian, $|\nabla \varepsilon_{\mathbf{k}}| = \sqrt{\sum_a v_a(\mathbf{k})^2} \equiv v(\mathbf{k})$, in converting the bulk integral into the integration $\oint_{\text{FS}} \bar{d}^2k$ on the Fermi surface.

We consider a Weyl (W^+) and an anti-Weyl (W^-) node, located on the k_x - k_y plane sketched in Fig. S14A (for the 3D Brillouin zone, see Fig. S15). The considered zincblende structure has a mirror symmetry M_{xy} , indicated by the dashed $k_x = k_y$ line in Fig. S14A. The dispersion of the Weyl-Kondo solution across W^+ and W^- , perpendicular to this line, is shown in Fig. S14B for the case where the Fermi energy is slightly away from the nodal energy (a close-up in energy of this dispersion is shown in Fig. 4B of the main part). M_{xy} reflects the Fermi pocket around W^+ onto that of W^- (see black Fermi surface contour lines in Fig. S14A). Under M_{xy} , \mathbf{k} and \mathbf{v} transform as vectors, while $\boldsymbol{\Omega}$ transforms as a pseudovector. Each component transforms as $k_{F,x/y}^{W-} \leftrightarrow k_{F,y/x}^{W+}$, $v_{x/y}^{W-} \leftrightarrow v_{y/x}^{W+}$, $\Omega_{x/y}^{W-} \leftrightarrow -\Omega_{y/x}^{W+}$. We find that, under M_{xy} , the contribution from the Fermi surface around W^+ and that from the Fermi surface around W^- are related to each other as $D_{xy}^{W+}(\mathbf{k}_F^{W+}) \leftrightarrow -D_{yx}^{W-}(\mathbf{k}_F^{W-})$. We can thus re-express D_{xy} as

$$D_{xy} = D_{xy}^{W+}(\mathbf{k}_F^{W+}) + D_{xy}^{W-}(\mathbf{k}_F^{W-}) = D_{xy}^{W+}(\mathbf{k}_F^{W+}) - D_{yx}^{W+}(\mathbf{k}_F^{W+}) = \oint_{\text{FS}}^{\text{W}^+} \bar{d}^2k \hat{\mathbf{z}} \cdot (\hat{\mathbf{v}} \times \boldsymbol{\Omega}) \quad , \quad (\text{S32})$$

where we have used Eqn. S31. The integral \oint is now only on the Fermi surface around the W^+ node. Here, $\hat{\mathbf{v}}$ represents the unit vector along the direction of the Fermi velocity vector, and $\boldsymbol{\Omega} = (\Omega_x \ \Omega_y \ \Omega_z)$. We note that, in addition to the ones of the $k_z = 2\pi$ plane we have discussed so far, Weyl/anti-Weyl nodes also exist on the planes $k_x = 2\pi$ and $k_y = 2\pi$. The M_{xy} operation

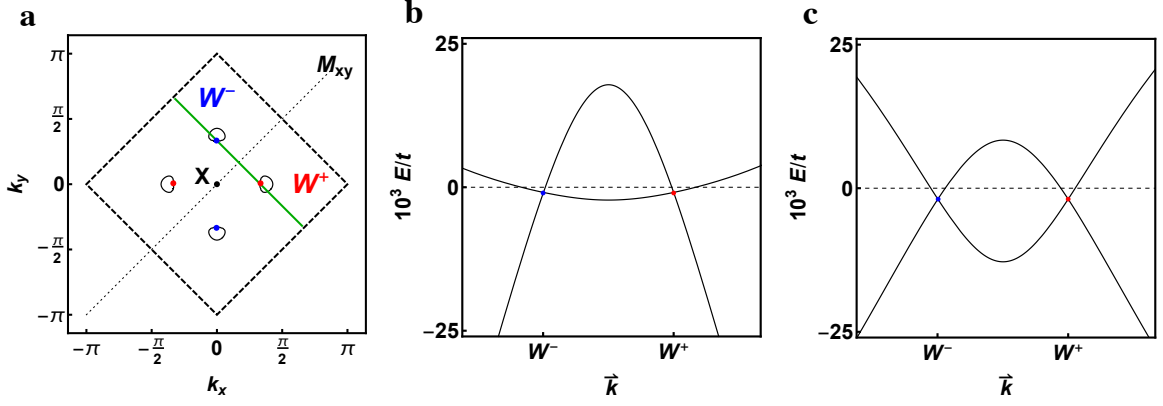


FIG. S14: **Fermi pockets and dispersion around pairs of Weyl nodes.** (A) k_x - k_y plane at the Brillouin zone boundary $k_z = 2\pi$, with two pairs of Weyl nodes as obtained for the tilted Weyl-Kondo semimetal model of Eqns. S23-S26, for the tilt parameter $C = 0.9$ and the Fermi energy slightly away from the nodal energy. The green line indicates a path through the Weyl node W^+ and the anti-Weyl node W^- perpendicular to the dotted $k_x = k_y$ line representing the M_{xy} mirror symmetry of the considered zincblende structure. The black contours are the 2D projections of Fermi pockets surrounding the nodes. (B) Dispersion along the green line in (A), with energy in units of t , the Fermi energy at $E/t = 0$, and for $C = 0.9$. (C) Corresponding dispersion without tilt ($C = 0$), as determined in ref [25].

relates the Weyl nodes on the $k_x = 2\pi$ plane to the anti-Weyl nodes on the $k_y = 2\pi$ plane. Thus, all these nodes contribute to the Berry curvature dipole according to Eqn. S32.

For a Weyl node without tilt, the Fermi surface is a sphere with the node in its center. The unit Fermi velocity \hat{v} in the integral in Eqn. S32 is then always parallel or antiparallel to the Berry curvature vector Ω , which results in $\hat{v} \times \Omega = 0$. In the presence of tilt, by contrast, $\hat{v} \times \Omega \neq 0$ at any momentum point on the Fermi surface because \hat{v} is not (anti)parallel to Ω . Moreover, because the Kondo effect places the Weyl/anti-Weyl nodes close to the Fermi energy, the Berry curvature Ω is very large on the Fermi surface, leading thus to very large values of D_{xy} .

It is straightforward to generalize Eqn. S32 for arbitrary directions. For the D_{yz} and D_{xz} components, we can utilize M_{yz} (M_{xz}) to arrive at similar results with $\hat{z} \rightarrow \hat{x}$ (\hat{y}). In general, D_{ab} can be written in a compact form as

$$D_{ab} = \oint_{\text{FS}}^{\text{W}^+} d^2k \hat{c} \cdot (\hat{v} \times \Omega) \quad , \quad (\text{S33})$$

where \hat{c} refers to the axis perpendicular to a and b .

Our experiments, however, have revealed a spontaneous Hall effect also in the first harmonic response and can thus not be explained by this weak-field treatment. In Sect. IV C below we show that, in the fully nonequilibrium regime, both the second and first harmonic response are allowed.

C. Berry curvature induced Hall response of titled Weyl-Kondo semimetal: Fully nonequilibrium regime

Weyl nodes are Berry curvature singularities. In the Weyl-Kondo semimetal phase, these nodes are pinned close to the Fermi energy [25]. This has two immediate consequences. First, the Berry curvature singularities dominate the electronic behavior. Second, the Fermi pockets are very small. In addition, for tilted Weyl cones, the Fermi surface is asymmetric with respect to the Weyl nodes and there will thus be directions along which the Weyl nodes are in extreme proximity (at a minimal distance denoted by k_W) to the Fermi surface, as is sketched in Fig. 4C of the main part. An applied electric field will then readily cause a shift $\Delta\mathbf{k}$ in the distribution function $f(\mathbf{k})$ that is sizeable compared to k_W , and possibly even compared to the Fermi wavevector k_F . This brings the system to the fully nonequilibrium regime (Fig. S15), where the perturbative treatment of Sect. IV B will fail.

In fact, an electric field $\mathcal{E} = \mathcal{E}_x(t)\hat{x}$ has a current response not only along the longitudinal x direction but, via [60]

$$v_{\text{an},y}(\mathbf{k}) = -\frac{e}{\hbar}\mathcal{E}_x(t)\Omega_z(\mathbf{k}) , \quad (\text{S34})$$

$$v_{\text{an},z}(\mathbf{k}) = \frac{e}{\hbar}\mathcal{E}_x(t)\Omega_y(\mathbf{k}) , \quad (\text{S35})$$

also along the transverse directions. In the Hall effect geometry, the ensuing transverse currents will set up transverse electric fields \mathcal{E}_y and \mathcal{E}_z . The total electric field will produce a distribution function

$$f(\mathbf{k}) = f_0(\mathbf{k}) + g(\mathbf{k}) , \quad (\text{S36})$$

that will be appreciably different from the equilibrium (Fermi-Dirac) distribution function $f_0(\mathbf{k})$, and even break the lattice symmetry (Fig. S15). Thus, an expansion around $f_0(\mathbf{k})$ will not be sufficient.

To delineate the relation to previous (perturbative) approaches [32], we distinguish a weak-field regime, where $\Delta k/k_F$ and $\Delta k/k_W$ are both $\ll 1$ (Fig. 4C left of the main part), and a fully

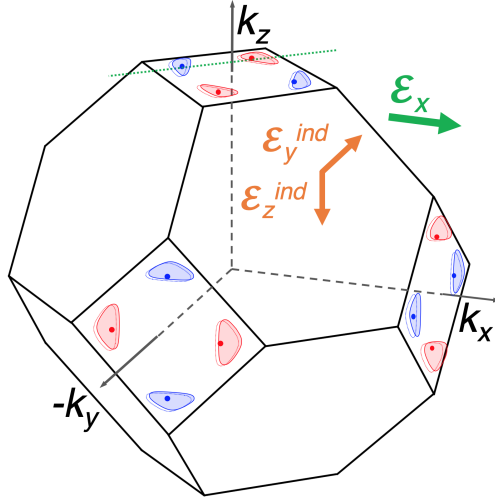


FIG. S15: **Electric field effect on the electron distribution in the fully nonequilibrium regime.** Schematic of the Brillouin zone (BZ) of the tilted Weyl-Kondo semimetal model of Sect. IV A, with the Weyl nodes shown as dots and the Fermi pockets projected to the BZ boundary indicated by red and blue dotted lines. The green dotted line indicates the cut shown in Fig. 4B of the main part. An electric field \mathcal{E}_x applied along the k_x direction induces, via the anomalous velocity $\mathbf{v}_{\text{an}} \sim \mathcal{E} \times \boldsymbol{\Omega}$, also transverse fields \mathcal{E}_y and \mathcal{E}_z . The proximity of the Weyl and anti-Weyl nodes to the Fermi surface implies that even an electric field small in absolute scale causes a nonperturbative change to the electron distribution, shifting its occupied part in all directions (red and blue shaded areas).

nonequilibrium regime where either of the two (or both) are no longer true (Fig. 4C right of the main part and Fig. S15). The reference point for the weak-field regime is $\mathcal{E} = 0$ (Fig. 4D of the main part), where the system is in equilibrium and the corresponding distribution function is $f_0(\mathbf{k})$, which is even in \mathbf{k} . Replacing $f(\mathbf{k})$ in

$$\sigma_{xy} = \frac{e^2}{\hbar} \int_{\mathbf{k}} f(\mathbf{k}) \Omega_z(\mathbf{k}) \quad (\text{S37})$$

by $f_0(\mathbf{k})$ (the zeroth order term of the Taylor expansion) leads to a vanishing result as $\Omega_z(\mathbf{k})$ is odd in \mathbf{k} . The first order term in the Taylor expansion, which is linear in \mathcal{E} , leads to a linear-in- \mathcal{E} Hall conductivity σ_{xy} and, via

$$\mathbf{j}_y = \sigma_{xy}(\boldsymbol{\mathcal{E}}) \cdot \boldsymbol{\mathcal{E}}_x \quad , \quad (\text{S38})$$

to a linear-in- \mathcal{E}^2 Hall current density j_y that corresponds to the 2ω contribution to σ_{xy} derived in

ref [32].

By contrast, in the fully nonequilibrium regime (Fig. 4C right and 4D of the main part and Fig. S15), $\Delta k/k_W$ (and possibly $\Delta k/k_F$ as well) not being small means that we can no longer expand $f(\mathbf{k})$ with respect to the equilibrium distribution. Instead, the reference point corresponds to a nonzero drive \mathcal{E} , where the distribution function $f(\mathbf{k})$ contains an odd-in- \mathbf{k} component. Inserting such an $f(\mathbf{k})$ term into Eqn. S37 leads to a nonzero value for the zeroth order term in σ_{xy} , and thus to a 1ω response as observed in our experiments. Accompanying it will be a 2ω (and an associated 0ω) response, that comes from the first-order term in the Taylor expansion of $f(\mathbf{k})$ with respect to the nonzero \mathcal{E} . Of course, a Taylor expansion around a nonzero field is again an approximation and, ultimately, $f(\mathbf{k})$ should be determined in a fully nonperturbative approach, which is a challenging task for future studies.

In summary, the appearance of the 1ω component of the spontaneous Hall response in the fully nonequilibrium regime is a new effect; it is distinct from the weak-field regime [32], where this component is absent. As stressed above, a Weyl-Kondo semimetal is readily—without applying electric fields that are large on absolute scales—in this regime due to its small Fermi pockets that asymmetrically surround the Weyl and anti-Weyl nodes.

-
- [24] S. Dzsaber, L. Prochaska, A. Sidorenko, G. Eguchi, R. Svagera, M. Waas, A. Prokofiev, Q. Si, S. Paschen, Kondo insulator to semimetal transformation tuned by spin-orbit coupling. *Phys. Rev. Lett.* **118**, 246601 (2017).
- [25] H.-H. Lai, S. E. Grefe, S. Paschen, Q. Si, Weyl-Kondo semimetal in heavy-fermion systems. *Proc. Natl. Acad. Sci. U.S.A.* **115**, 93 (2018).
- [29] N. Nagaosa, J. Sinova, S. Onoda, A. H. MacDonald, N. P. Ong, Anomalous Hall effect. *Rev. Mod. Phys.* **82**, 1539 (2010).
- [32] I. Sodemann, L. Fu, Quantum nonlinear Hall effect induced by Berry curvature dipole in time-reversal invariant materials. *Phys. Rev. Lett.* **115**, 216806 (2015).
- [35] Y. Zhang, Y. Sun, B. Yan, Berry curvature dipole in Weyl semimetal materials: An *ab initio* study. *Phys. Rev. B* **97**, 041101 (2018).
- [39] A. Fert, P. M. Levy, Theory of the Hall effect in heavy-fermion compounds. *Phys. Rev. B* **36**, 1907 (1987).

- [40] M. F. Hundley, A. Malinowski, P. G. Pagliuso, J. L. Sarrao, J. D. Thompson, Anomalous f -electron Hall effect in the heavy-fermion system $CeTIn_5$ ($T = Co, Ir, \text{ or } Rh$). *Phys. Rev. B* **70**, 035113 (2004).
- [41] S. Paschen, T. Lühmann, S. Wirth, P. Gegenwart, O. Trovarelli, C. Geibel, F. Steglich, P. Coleman, Q. Si, Hall-effect evolution across a heavy-fermion quantum critical point. *Nature* **432**, 881 (2004).
- [42] J. Custers, K. Lorenzer, M. Müller, A. Prokofiev, A. Sidorenko, H. Winkler, A. M. Strydom, Y. Shimura, T. Sakakibara, R. Yu, Q. Si, S. Paschen, Destruction of the Kondo effect in the cubic heavy-fermion compound $Ce_3Pd_{20}Si_6$. *Nat. Mater.* **11**, 189 (2012).
- [43] S. K. Kushwaha, M. K. Chan, J. Park, S. M. Thomas, E. D. Bauer, J. D. Thompson, F. Ronning, P. F. S. Rosa, N. Harrison, Magnetic field-tuned Fermi liquid in a Kondo insulator. *Nat. Commun.* **10**, 5487 (2019).
- [44] L. Berger, Side-jump mechanism for the Hall effect of ferromagnets. *Phys. Rev. B* **2**, 4559 (1970).
- [45] G. Eguchi, S. Paschen, Robust scheme for magnetotransport analysis in topological insulators. *Phys. Rev. B* **99**, 165128 (2019).
- [46] G. M. Luke, Y. Fudamoto, K. M. Kojima, M. I. Larkin, J. Merrin, B. Nachumi, Y. J. Uemura, Y. Maeno, Z. Q. Mao, Y. Mori, H. Nakamura, M. Sigrist, Time-reversal symmetry-breaking superconductivity in Sr_2RuO_4 . *Nature* **394**, 558 (1998).
- [47] A. D. Hillier, J. Quintanilla, R. Cywinski, Evidence for time-reversal symmetry breaking in the non-centrosymmetric superconductor $LaNiC_2$. *Phys. Rev. Lett.* **102**, 117007 (2009).
- [48] T. Shang, G. M. Pang, C. Baines, W. B. Jiang, W. Xie, A. Wang, M. Medarde, E. Pomjakushina, M. Shi, J. Mesot, H. Q. Yuan, T. Shiroka, Nodeless superconductivity and time-reversal symmetry breaking in the noncentrosymmetric superconductor $Re_{24}Ti$. *Phys. Rev. B* **97**, 020502 (2018).
- [49] A. Yaouanc, P. Dalmas de Réotier, *Muon Spin Rotation, Relaxation, and Resonance: Applications to Condensed Matter* (Oxford University Press, Oxford, 2011).
- [50] A. A. Suter, B. M. Wojek, Musrfit: A free platform-independent framework for μ SR data analysis. *Phys. Procedia* **30**, 69 (2012).
- [51] P. Blaha, K. Schwarz, G. K. H. Madsen, D. Kvasnicka, J. Luitz, R. Laskowski, F. Tran, L. Marks, Wien2k, an augmented plane wave plus local orbital program for calculating the crystal properties, TU Vienna, Austria (2018). <http://www.wien2k.at>.
- [52] J. P. Perdew, K. Burke, M. Ernzerhof, Generalized gradient approximation made simple. *Phys. Rev. Lett.* **77**, 3865 (1996).
- [53] W. Hermes, S. Linsinger, R. Mishra, R. Pöttgen, Structure and properties of $Ce_3Pd_3Bi_4$, $CePdBi$, and

- CePd₂Zn₃. *Monatsh. Chem.* **139**, 1143 (2008).
- [54] S. J. Ahmed, J. Kivinen, B. Zaporzan, L. Curiel, S. Pichardo, O. Rubel, BerryPI: A software for studying polarization of crystalline solids with WIEN2k density functional all-electron package. *Comput. Phys. Commun.* **184**, 647 (2013).
- [55] H. Weng, C. Fang, Z. Fang, B. A. Bernevig, X. Dai, Weyl semimetal phase in noncentrosymmetric transition-metal monophosphides. *Phys. Rev. X* **5**, 011029 (2015).
- [56] J. M. Tomczak, Thermoelectricity in correlated narrow-gap semiconductors. *J. Phys.: Condens. Matter* **30**, 183001 (2018).
- [57] C. Cao, G.-X. Zhi, J.-X. Zhu, From trivial Kondo insulator Ce₃Pt₃Bi₄ to topological nodal-line semimetal Ce₃Pd₃Bi₄. *Phys. Rev. Lett.* **124**, 166403 (2020).
- [58] S. E. Grefe, H.-H. Lai, S. Paschen, Q. Si, Weyl-Kondo semimetals in nonsymmorphic systems. *Phys. Rev. B* **101**, 075138 (2020).
- [59] A. C. Hewson, *The Kondo Problem to Heavy Fermions* (Cambridge University Press, Cambridge, 1997).
- [60] G. Sundaram, Q. Niu, Wave-packet dynamics in slowly perturbed crystals: Gradient corrections and Berry-phase effects. *Phys. Rev. B* **59**, 14915 (1999).